

Journal Pre-proof

A comparative study on effective density, shape factor, and volatile mixing of non-spherical particles using tandem aerodynamic diameter, mobility diameter, and mass measurements

Mohsen Kazemimanesh, Md Mostafizur Rahman, Dumitru Duca, Tyler J. Johnson, Ahmed Addad, George Giannopoulos, Cristian Focsa, Adam M. Boies

PII: S0021-8502(21)00655-8

DOI: <https://doi.org/10.1016/j.jaerosci.2021.105930>

Reference: AS 105930

To appear in: *Journal of Aerosol Science*

Received Date: 18 May 2021

Revised Date: 13 October 2021

Accepted Date: 10 December 2021

Please cite this article as: Kazemimanesh M, Rahman MM, Duca D, Johnson TJ, Addad A, Giannopoulos G, Focsa C, Boies AM, A comparative study on effective density, shape factor, and volatile mixing of non-spherical particles using tandem aerodynamic diameter, mobility diameter, and mass measurements, *Journal of Aerosol Science* (2022), doi: <https://doi.org/10.1016/j.jaerosci.2021.105930>.

This is a PDF file of an article that has undergone enhancements after acceptance, such as the addition of a cover page and metadata, and formatting for readability, but it is not yet the definitive version of record. This version will undergo additional copyediting, typesetting and review before it is published in its final form, but we are providing this version to give early visibility of the article. Please note that, during the production process, errors may be discovered which could affect the content, and all legal disclaimers that apply to the journal pertain.

© 2021 Published by Elsevier Ltd.



A comparative study on effective density, shape factor, and volatile mixing of non-spherical particles using tandem aerodynamic diameter, mobility diameter, and mass measurements

Mohsen Kazemimanesh^{a,*}, Md Mostafizur Rahman^{a,1}, Dumitru Duca^b, Tyler J. Johnson^a, Ahmed Addad^c, George Giannopoulos^a, Cristian Focsa^b, Adam M. Boies^a

^aUniversity of Cambridge, Department of Engineering, Cambridge, CB2 1PZ, United Kingdom

^bUniversity of Lille, CNRS, UMR 8523 – Laboratory of Physics of Lasers, Atoms and Molecules (PhLAM), F-59000 Lille, France

^cUniversity of Lille, CNRS, UMR 8207 – Materials and Transformations Unit (UMET), F-59000 Lille, France

*Corresponding author. E-mail address: mk2054@cam.ac.uk, Address: Hopkinson Lab, Division A, Department of Engineering, University of Cambridge, Trumpington Street, Cambridge, CB2 1PZ, United Kingdom

¹ Present address: School of Mechanical, Aerospace and Automotive Engineering, Coventry University, Coventry, CV1 5FB, United Kingdom

A comparative study on effective density, shape factor, and volatile mixing of non-spherical particles using tandem aerodynamic diameter, mobility diameter, and mass measurements

Abstract

Combustion-generated particles are typically non-spherical (soot aggregates) and sometimes mixed with organic compounds (*e.g.* in vehicle emissions). The effective density, dynamic shape factor, and volatile mixing of particles are widely studied using aerosol instruments that measure the particle mobility diameter, aerodynamic diameter, and mass. In theory, any of these three physical properties can be obtained from a combination of the other two. In the present study, a tandem arrangement of aerodynamic aerosol classifier (AAC; measuring aerodynamic diameter), differential mobility analyzer (DMA; measuring mobility diameter), optional catalytic stripper (CS), and centrifugal particle mass analyzer (CPMA; measuring particle mass) was used to study the effective density, dynamic shape factor, and volatile mixing of non-spherical non-homogenous particles. In terms of mass, the vast majority of the particles were purely semi-volatile mixed with soot with and without semi-volatile coating. The effective density of polydisperse non-stripped particles was relatively constant (indicating nearly spherical particles), while that of polydisperse stripped particles decreased from ~ 1200 to ~ 800 kg/m^3 as the particle size increased (indicating a compact structure). The effective density of monodisperse particles, measured by DMA-CPMA, AAC-DMA, and AAC-CPMA methods, was consistent within the measurement uncertainty; however, the latter method had larger discrepancy with the other two methods, particularly for non-spherical particles. The dynamic shape factor, measured by AAC-CPMA and DMA-CPMA methods, increased with the mobility diameter, a trend also supported by electron micrographs. The volatile mass fraction of particles decreased as their mobility diameter increased, with smaller particles having volatile mass fraction of $\sim 20\%$. This result was further confirmed by chemical characterization of size-selected particles, proving the robustness of online aerosol measurements.

1. Introduction

Particulate matter (PM) emissions from anthropogenic combustion sources such as vehicles are the focus of extensive research due to their negative impacts on global climate (Bond et al., 2013; Jacobson, 2001; Ramanathan & Carmichael, 2008), local and regional air quality

(Gaffney & Marley, 2009), and human health (Grahame et al., 2014; Janssen et al., 2011; Lim et al., 2012). Combustion-generated PM emissions commonly consist of solid carbonaceous spherules in aggregate structure—known as soot. Soot particles travel over long distances in the atmosphere, mixing with other aerosols or acting as condensation sites for organic compounds, sulfate, and nitrate along the way (Adachi & Buseck, 2008). Similarly, vehicle PM emissions in diluted and cooled state comprise of soot coated with condensed organic compounds—from unburned fuel and/or lubricating oil (Collura et al., 2005)—and sulfate, along with nucleated particles of condensed hydrocarbons and sulfate (Maricq, 2007).

The morphological properties of PM emissions are important parameters in estimating their transport and dispersion in the air. Moreover, morphology of soot aggregates may have an impact on how these particles can affect human health via their pulmonary toxicity (Bérubé et al., 1999). Morphology of aggregate particles can be characterized by several parameters, such as their fractal dimension, number and size of primary particles, and radius of gyration. Although effective density and dynamic shape factor are not *intrinsic* morphological parameters as they depend on Knudsen number, these parameters can still provide useful information about the morphology of PM emissions at ambient conditions. Kazemimanesh et al. (2019), Olfert and Rogak (2019), and Trivanovic et al. (2020) have shown that tandem measurement of effective density (or mass-mobility) can provide equivalent information about the morphology of soot particles (*e.g.* the power-law scaling relationship between aggregate size and primary particle size) as off-line analysis of electron micrographs of a large number of particles. Moreover, effective density of an aggregate particle can be an indicator of its structure compactness (Olfert & Rogak, 2019). Effective density is also an important parameter that can determine particle transport properties, provide a relationship between mobility and aerodynamic diameters of the particle, and be used to convert the particle size distribution to mass distribution and vice versa (Olfert et al., 2007). Dynamic shape factor for non-spherical

particles is used to determine the drag force on these particles (Hinds, 1999, p. 51), to predict their transport in the air or under the influence of force fields (*e.g.* gravity or electric), and—in the case of aggregate particles—may indicate the level of compactness in the aggregate structure (DeCarlo et al., 2004). Thus, real-time measurement of effective density and shape factor can provide indicators for the morphology of PM emissions.

The climatic impact of particles is enhanced by the organic and inorganic materials internally mixed with soot particles, which can enhance the absorption of sunlight through the *lensing effect* (Cappa et al., 2012; China et al., 2013; Liu et al., 2015; Peng et al., 2016). The type of material mixed with soot, the coating thickness, and the morphology of soot can affect the lensing effect (Dickau et al., 2016; Liu et al., 2015; Thamban et al., 2017). The light absorption enhancement for a soot aggregate with coating has been shown to scale with the ratio of total mass of particle to mass of soot, *i.e.* $m_{\text{total}}/m_{\text{soot}}$ (Chakrabarty & Heinson, 2018). Thus, to estimate the radiative forcing due to soot coated with organics, the amount of organic compounds and their mass fraction needs to be measured. The amount of organic compounds in PM emissions are often measured by offline methods such as mass spectrometry and chromatography (Collura et al., 2005; Schmitt-Kopplin et al., 2010). Offline methods require collecting and handling samples and lack real-time information about the total amount and mass fraction of organic compounds. Online measurement methods, such as using aerosol instruments, may accurately quantify the volatile mass fraction of PM emissions, *i.e.* the mass of semi-volatile compounds to the total mass of PM.

In previous studies, aerosol instruments that classify particles based on mobility diameter, mass, and aerodynamic diameter have been widely used to determine the morphology and volatile mass fraction of aerosol particles from different sources. As will be shown in Section 2, any pairwise combination of mobility diameter, mass, and aerodynamic diameter can be used to determine particle morphology. McMurry et al. (2002), Park et al. (2003), and

Barone et al. (2011) used differential mobility analyzer (DMA) and aerosol particle mass analyzer (APM) in tandem to measure the effective density of atmospheric particles and diesel soot. Xue et al. (2009) used the DMA-APM arrangement to measure the effective density and shape factor of soot particles with and without coating of dicarboxylic acids. In several other studies, tandem arrangement of DMA, optional catalytic stripper or thermodenuder, and centrifugal particle mass analyzer (CPMA) has been employed to measure the effective density and/or volatile mass fraction of aerosol particles from various combustion sources (e.g. Cross et al., 2010; Ghazi et al., 2013; Graves et al., 2017, 2020; Kazemimanesh et al., 2019, 2021; Momenimovahed & Olfert, 2015; Olfert et al., 2007; Quiros et al., 2015; Trivanovic et al., 2020). Tavakoli and Olfert (2014) used aerodynamic aerosol classifier (AAC) and DMA in tandem to measure the dynamic shape factor and effective density of soot particles from an inverted-flame burner. Other studies have used aerosol mass spectrometer (AMS) along with DMA to derive the dynamic shape factor of flame soot with and without organic coating based on particle mobility diameter and vacuum aerodynamic diameter (Slowik et al., 2004; Slowik, Cross, Han, Davidovits, et al., 2007).

Despite the growing interest in using the above-mentioned aerosol instruments to study particle morphology, a systematic inter-comparison of different combinations of instruments with a single source of particles has been critically lacking. Yao et al. (2020) used nearly spherical solid particles (ammonium sulfate or collapsed carbon black mimic) and employed pairwise combinations of AAC, DMA, and APM to derive the particle effective density and dynamic shape factor. In this study we use non-spherical soot particles with and without semi-volatile coating and employ for the first time a unique set of aerosol instruments—AAC, DMA, CPMA, and catalytic stripper—in tandem to compare the morphological parameters (*i.e.* effective density, dynamic shape factor, and volume equivalent diameter) and volatile mass fraction of particles. Using this tandem measurement technique, different combinations of

instruments can be used to determine each of the above-mentioned parameters. For instance, the effective density of particles can be obtained from either of DMA-CPMA, AAC-DMA, or AAC-CPMA tandem arrangements. For homogeneous spherical particles, *e.g.* those used in Yao et al. (2020), being monodisperse in one domain (such as aerodynamic diameter) means that the particles are monodisperse in other domains (such as mobility diameter and mass) as well. However, this simple mapping between particle properties no longer occurs for non-spherical and/or non-homogenous particles (Johnson et al., 2021). In the current study, combustion engine PM emissions with non-spherical morphology (soot aggregates) and non-homogeneity (semi-volatile coating on soot particles) are investigated. The objective of this study is to compare the morphology of non-spherical particles, as indicated by effective density or dynamic shape factor, obtained from various instrument combinations and to discuss the accuracy of each measurement technique. The results of this study are useful for researchers to determine the most accurate combination of instruments available to them when studying the morphology of non-spherical and/or mixed aerosol particles.

2. Theory

The electrical mobility of a particle, Z_p , is defined as the velocity of the charged particle in an electric field of unit strength (Hinds, 1999, p. 322) and is given by

$$Z_p = \frac{V_{TE}}{E} \quad (1)$$

where V_{TE} is the terminal electrostatic velocity and E is the electric field intensity. The DMA classifies particles based on their electrical mobility by balancing the drag and electric forces exerted on the particles. The mobility equivalent diameter of a particle, d_m , is the diameter of a spherical particle with the same electrical mobility as the target particle and is derived from the electrical mobility measurement by

$$Z_p = \frac{neC_c(d_m)}{3\pi\mu d_m} \quad (2)$$

where e is the elementary charge (1.61×10^{-19} C), n is the number of elementary charges on the particle, C_c is the Cunningham slip correction factor, and μ is the gas viscosity. Mechanical mobility (or simply, mobility) of a particle, B , in Stokes regime ($Re < 1$) is defined as the ratio of the terminal velocity, V_T , of a particle to the drag force, F_D , acting on the particle, *i.e.* $B = V_T/F_D$ (Hinds, 1999, p. 47). Mobility of a particle can be related to its electrical mobility as follows:

$$B = \frac{Z_p}{ne} \quad (3)$$

The AAC uses the balance of drag and centrifugal forces on the particles and classifies them based on their relaxation time, τ , which is defined as the product of particle mass, m , and mobility as follows:

$$\tau = mB. \quad (4)$$

Particle relaxation time can be used to derive particle aerodynamic diameter, d_a , by

$$\tau = \frac{\rho_0 d_a^2 C_c(d_a)}{18\mu} \quad (5)$$

where ρ_0 is the standard particle density (1000 kg/m^3).

An important concept in studying the particle morphology is the dynamic shape factor, which is derived from the volume equivalent diameter. The volume equivalent diameter of a particle, d_{ve} , is the diameter of a spherical particle having the same volume as that of a non-spherical particle. From this definition, d_{ve} can be obtained from

$$d_{ve} = \left(\frac{6m}{\pi\rho_p} \right)^{1/3} \quad (6)$$

where ρ_p is the particle material density. The CPMA uses the balance of centrifugal and electric forces on the particles and classifies them based on their mass to charge ratio. Thus, the mass of singly charged particles can be measured by the CPMA directly. Alternatively, the mass of a particle can be obtained by combining Eq. (3) and (4) as follows

$$m = \frac{ne\tau}{Z_p} \quad (7)$$

Thus, by measuring particle relaxation time and electrical mobility and combining Eq. (6) and (7), d_{ve} can also be obtained from

$$d_{ve} = \left(\frac{6ne\tau}{\pi\rho_p Z_p} \right)^{1/3} \quad (8)$$

The dynamic shape factor, χ , is defined as the ratio of drag force, F_D , on a non-spherical particle to that of a spherical particle having the same volume and velocity as the non-spherical particle (Hinds, 1999, p. 51) and in Stokes regime is given by

$$\chi = \frac{F_D}{F_{D,ve}} = \frac{F_D}{3\pi\mu v d_{ve}} \quad (9)$$

where v is the velocity of the particle. For spherical particles $\chi = 1$ and $d_m = d_{ve}$, while for non-spherical particles $\chi > 1$ and $d_m > d_{ve}$. Similar to Eq. (5), the particle relaxation time can be expressed in terms of its volume equivalent diameter as follows

$$\tau = \frac{\rho_p d_{ve}^2 C_c(d_{ve})}{18\mu\chi} \quad (10)$$

Moreover, by equating the drag and electrostatic forces acting on a non-spherical particle moving at constant velocity in an electric field (Eq. (1) and (9)), we can obtain an expression for the particle electrical mobility in terms of its volume equivalent diameter (Tavakoli & Olfert, 2014) as follows

$$Z_p = \frac{neC_c(d_{ve})}{3\pi\mu d_{ve}\chi} \quad (11)$$

Dynamic shape factor can be obtained from re-arranging either Eq. (10) or (11) in the following forms

$$\chi = \frac{\rho_p d_{ve}^2 C_c(d_{ve})}{18\mu\tau} \quad (12)$$

$$\chi = \frac{neC_c(d_{ve})}{3\pi\mu d_{ve} Z_p} \quad (13)$$

The particle volume equivalent diameter in Eq. (12) and (13) can be obtained from Eq. (6).

Alternatively, one can obtain χ by equating Eq. (2) and (11) for electrical mobility as follows

$$\chi = \frac{d_m}{d_{ve}} \cdot \frac{C_c(d_{ve})}{C_c(d_m)} \quad (14)$$

This relationship uses derived parameters of d_m (from Z_p) and d_{ve} (from m) rather than directly measured parameters.

Similar to Eq. (5), the particle relaxation time can be expressed in terms of particle mobility diameter as follows:

$$\tau = \frac{\rho_{\text{eff}} d_m^2 C_c(d_m)}{18\mu} \quad (15)$$

where ρ_{eff} is the effective density of the particle. The effective density of a particle is defined as the particle mass divided by the volume of a sphere having the same diameter as the mobility diameter of the particle (McMurry et al., 2002)

$$\rho_{\text{eff}} = \frac{m}{\frac{\pi}{6} d_m^3} = \rho_p \left(\frac{d_{ve}}{d_m} \right)^3 \quad (16)$$

Thus, the effective density of a non-spherical particle is less than its true material density because $d_{ve} < d_m$. One can measure the effective density of a particle by measuring its mass and mobility diameter using CPMA and DMA, respectively. It should be noted that the definition of effective density based on particle mass and mobility diameter—which is used throughout this study—is the most common form of effective density used in the literature, although other definitions also exist (DeCarlo et al., 2004). The effective density of a particle can also be obtained by equating Eq. (5) and (15), which is given by

$$\rho_{\text{eff}} = \rho_0 \frac{d_a^2 C_c(d_a)}{d_m^2 C_c(d_m)} \quad (17)$$

By measuring particle aerodynamic and mobility diameters using AAC and DMA, respectively, the effective density of the particle can be obtained from Eq. (17). The third method to obtain the particle effective density is by combining Eq. (16) and (17), which results in

$$\rho_{\text{eff}} = \left(\frac{\pi d_a^3}{6m} \right)^2 \left(\frac{\rho_0 C_c(d_a)}{C_c(d_m)} \right)^3 \quad (18)$$

By measuring the particle aerodynamic diameter, mobility diameter, and mass using AAC, DMA, and CPMA, respectively, the effective density of the particle can be determined. Details of the uncertainty analysis for the effective densities calculated from Eq. (16)–(18) are reported in the Supplementary Material.

3. Experimental setup

Figure 1 shows the schematic of the experimental set up which was developed at Bosch GmbH facilities. The particle source used in this study was a single-cylinder gasoline direct injection (GDI) engine (specifications in the Supplementary Material), which generated non-spherical non-homogeneous particles typical of PM emissions from vehicles, *i.e.* soot particles with organic coating along with nucleated semi-volatile particles. The fuel used to run the engine was Euro Stage V E5 gasoline (CEC-RF-02-08 E5), which was injected at 270° before top dead center at $\lambda = 1.01^2$. The temperature of coolant and oil (Agip SIGMA, 10W-40) was kept at 80°C . The particles were generated under two engine operating conditions: rotational speed of 2000 rpm at an indicated mean effective pressure (IMEP) of 6 bar (corresponding to a torque of 21.4 N·m or power of 28 kW) and rotational speed of 1200 rpm at an IMEP of either 12 bar (corresponding to a torque of 43 N·m or power of 34 kW) or 6 bar (corresponding to a torque of 21.4 N·m or power of 17 kW). Hereinafter, we refer to the IMEP of the engine as the engine load. To avoid contamination of the combustion chamber, the engine was conditioned with methane (CH_4) prior to changing the operating point. To avoid water vapor condensation and particle coagulation during sampling, the particles sampled from the engine exhaust were immediately (via an insulated 5-cm line) diluted with dry, particle-free compressed air using a

² λ is the ratio of the actual air-to-fuel ratio, AFR_{act} , to that of the stoichiometric condition, AFR_{stoich} , *i.e.* $\lambda = AFR_{\text{act}}/AFR_{\text{stoich}}$.

diluter (Dekati Ltd., Model FPS-4000). The diluter consisted of a perforated tube and an ejector diluter with an overall dilution ratio of $\sim 30:1$ and was kept constant for all tests. The diluter also reduced the temperature of the sample close to ambient temperature. Controlling the temperature of sample lines is necessary until the sample is diluted as the aerosol instruments cannot be operated at elevated temperatures. Thus, heated sample lines were not used downstream of the diluter. The sample lines between the Dekati diluter and different configurations were typically 40–50 cm long.

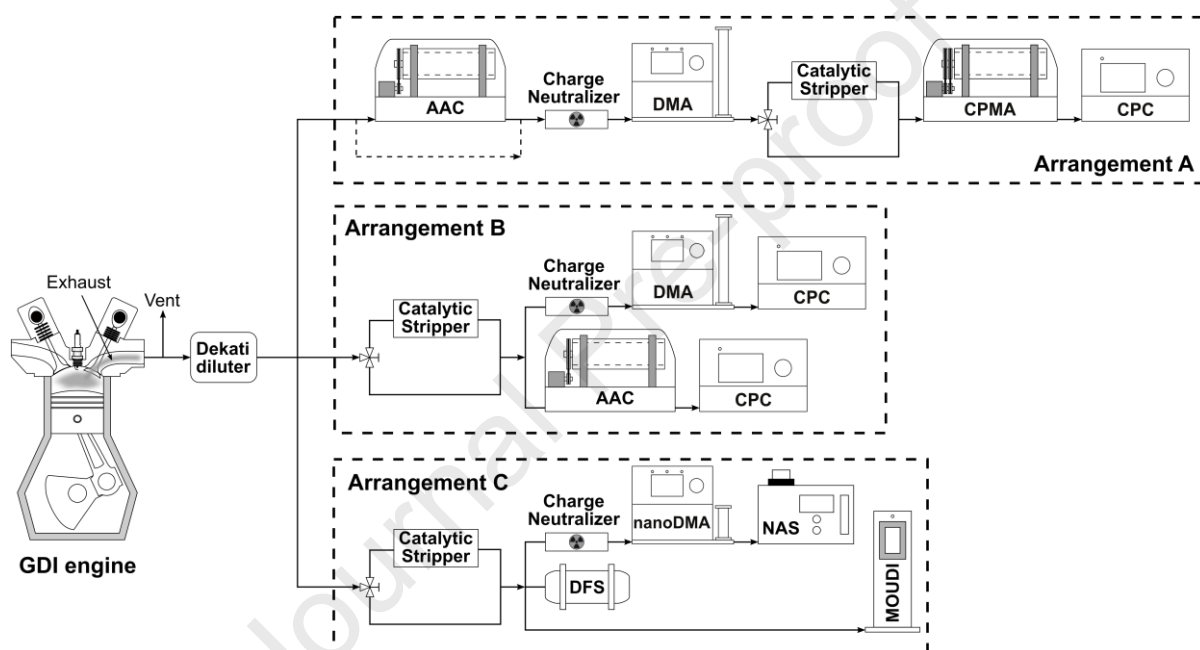


Figure 1: Schematic representation of the experimental setup. A fraction of the exhaust of the GDI engine is diluted and subsequently forwarded to various instruments shown in Arrangements A, B, and C. In arrangement A, the on-line characterization of particle morphology (in terms of effect density and dynamic shape factor) was performed with a tandem arrangement of AAC, DMA, optional catalytic stripper (CS), CPMA, and CPC. In Arrangement B, the mobility and aerodynamic size distributions of non-stripped and stripped particles were measured using the DMA-CPC and the AAC-CPC, respectively. In Arrangement C, particles were collected for off-line (chemical and morphological) characterization. A Nano-MOUDI cascade impactor and a combination of a nano-DMA and a nanometer aerosol sampler (NAS) were used to collect size-selected particles. A home-built double-filter sampler (DFS) (Ngo et al., 2020) separated and collected both polydisperse particles and gas-phase semi-volatiles.

As shown in Arrangement A (Figure 1), an AAC (Cambustion Ltd.), a DMA (TSI Inc., Model 3081), a CPMA (Cambustion Ltd.), and a condensation particle counter (CPC; TSI Inc., Model 3776) were used in tandem to study the effective density, dynamic shape factor, and volatile mixing state of the sampled particles. The effective density and dynamic shape factor

were determined from pairwise combination of these instruments (*i.e.* from either of DMA-CPMA, AAC-DMA, and AAC-CPMA) as explained below and were compared subsequently. A catalytic stripper (CS; Catalytic Instruments GmbH, Model CS-015) operating at 350 °C was used downstream of the DMA and upstream of the CPMA to study the morphology of non-stripped particles (that bypassed the CS) versus stripped particles (that passed through the CS). The CS removes any semi-volatile substances mixed internally or externally with the particles by evaporation and subsequent oxidation, leaving the non-volatile core in the downstream. The approach of using the CS downstream of the DMA is similar to other tandem classifier measurements, which select particles of interest, then vary the aerosol conditions and measure the effect on the particles. For example, Dickau et al. (2016) used a DMA-CS-CPMA to measure the volatile mixing of an aerosol, while Johnson et al. (2015) used a DMA-Dryer/Humidifier-CPMA and DMA to measure the hygroscopicity of an aerosol. The AAC classifies particles based on their relaxation time, from which the aerodynamic diameter of the particle can be derived (see Section 2). The DMA classifies particles based on their electrical mobility, from which the particle mobility diameter can be obtained as mentioned in Section 2. The CPMA classifies particles based on their mass to charge ratio. All classifiers (AAC, CPMA, and DMA) select particles of an average value of the respective particle property (τ , m , or Z_p) because these instruments have transfer functions with specific widths. Given that all classifier set points and fitted distributions are averages, all subsequently reported parameters, such as effective density, mass, equivalent diameters (d_a , d_m , d_{ve}), and dynamic shape factor are also averages of the classified particles. The CPC downstream of the CPMA measures the particle number concentration, N , which is used to obtain the mass spectral density of the particles ($dN/d\log m_p$, *i.e.*, number distribution of particles in each particle mass bin, m_p).

By bypassing the AAC in Arrangement A (dashed line in Figure 1), the DMA was used to select particles with a specific mobility diameter. Mobility-selected particles are then either

passed through or around the CS. The effluent of the CS was subsequently directed to the CPMA-CPC, which produced a mass spectral density for each specific mobility diameter. In addition to a main peak for singly-charged particles in the mass spectral density, particles with multiple charges would appear as separate peaks at specific size (and mass), which can be deconvoluted using a lognormal distribution with multiple modes. Furthermore, mobility-selected particles with different densities (*e.g.* completely semi-volatile vs. completely solid soot) may appear as separate peaks in the mass spectral density. Representative raw data plots for the mass spectral densities of non-stripped and stripped particles are shown in the Supplementary Material (as Figures S1 and S2). In this study, all mass spectral densities had an apparent unimodal form, without additional peaks due to particles with different densities or with multiple charges (majority of particles were < 100 nm and had a low fraction of multiple charging – see Section 4.1). Thus, the mass spectral densities were fitted with a unimodal lognormal function. The average mass of a singly-charged particle was obtained by finding the median of this lognormal fit. Note that although non-stripped particles were a mixture of two particle species (semi-volatile particles and non-volatile soot particles) as will be shown later, their corresponding mass spectral density did not have distinct peaks for each species. This was due to the fact that the density of non-volatile soot particles was close to that of semi-volatile particles in this study (as will be discussed in Sections 4.3 and 4.5) and both particle species were present in the single peak.

The average mass of a non-stripped particle with a selected mobility diameter, $m_{\text{ns}}(d_m)$, and the average mass of a stripped particle with the same mobility diameter, $m_{\text{s}}(d_m)$, can be used to determine the volatile mass fraction of the particle, $f_{\text{m,v}}$, as follows

$$f_{\text{m,v}}(d_m) = \frac{m_{\text{ns}}(d_m) - m_{\text{s}}(d_m)}{m_{\text{ns}}(d_m)} = 1 - \frac{m_{\text{s}}(d_m)}{m_{\text{ns}}(d_m)}. \quad (19)$$

In determining the volatile mass fraction of a particle, we assume that the particle has a non-volatile core (such as soot) which does not evaporate or oxidize in the heated CS. The volatile

mass fraction is a measure of semi-volatile species that are internally mixed (*i.e.* adsorbed as coating) with non-volatile species in a given particle. As will be shown shortly, it is also plausible that a fraction of particles is semi-volatile (such as nucleated particles in the PM emissions) and are completely removed in the CS.

Using the AAC upstream of the DMA-CPMA in Arrangement A, the aerodynamic diameter, mobility diameter, and mass of the sampled particles were measured in tandem. Figure 2 shows representative raw data plots of AAC-DMA-CPMA tandem measurements. Particles were first size selected based on their aerodynamic diameter by the AAC for this set of measurements, which are subsequently characterized by the DMA-CPMA-CPC arrangement as described earlier. Although the AAC provided a narrow aerodynamic diameter size distribution for each size selection by the AAC, the corresponding mobility diameter size distribution was slightly wider. Therefore, for each particle aerodynamic diameter selected by the AAC (*e.g.*, 50 nm), three mobility diameters (*e.g.*, 45, 50, and 55 nm) were selected by the DMA and the particle mass was measured using the CPMA, provided there were sufficiently high particle concentrations for transmission through the CPMA. The CS was used to characterize the mass of these size selected particles in stripped versus non-stripped conditions.

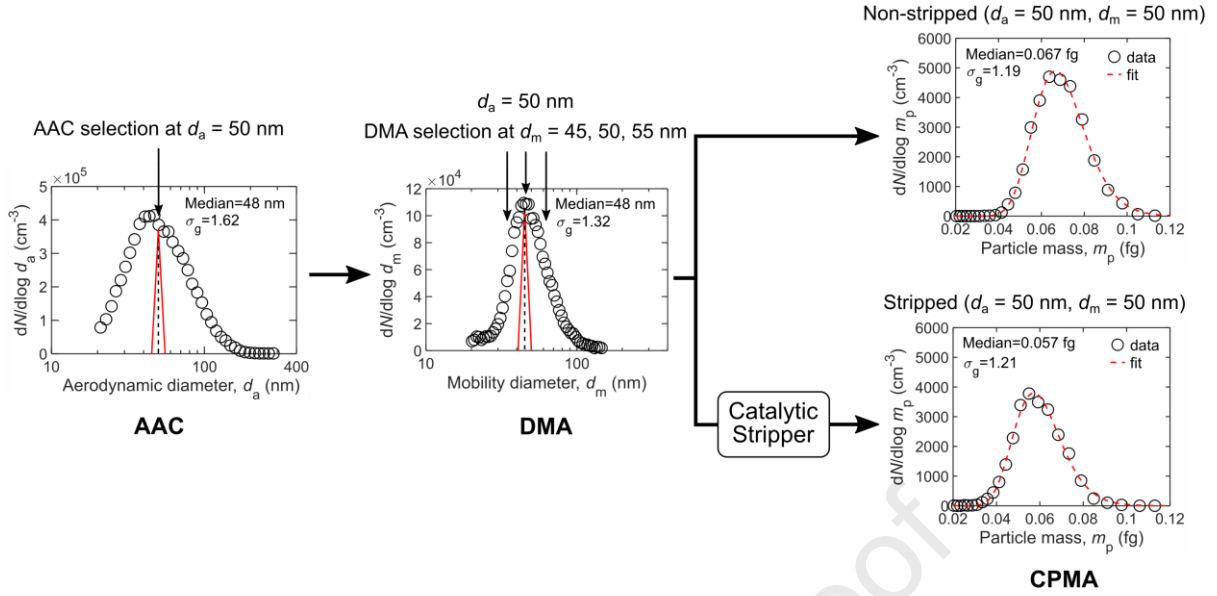


Figure 2: Representative raw data plots of AAC-DMA-CPMA tandem measurements. From a polydisperse population on the left ($\sigma_g = 1.62$), particles were selected at aerodynamic diameter of 50 nm using the AAC (the transfer function is shown as a red triangle). The monodisperse particles with $d_a = 50$ nm had a relatively wide ($\sigma_g = 1.32$) mobility diameter size distribution and were further size selected based on mobility diameter at either 45, 50, and 55 nm using the DMA (again, the transfer function is shown as a red triangle). Subsequently the mass spectral densities of non-stripped or stripped particles were measured by the CPMA (shown here is the case of $d_m = 50$ nm). Note that monodisperse particles in terms of their aerodynamic and mobility diameters had a mass spectral density with $\sigma_g \sim 1.20$, highlighting that non-spherical particles that are monodisperse in one property are not monodisperse in other properties.

Arrangement B in Figure 1 was used to measure the overall particle mobility diameter size distribution using the DMA and the CPC (following S. C. Wang & Flagan, 1990) and to measure the overall particle aerodynamic diameter size distribution using the AAC and the CPC (following Johnson et al., 2018). The CS was used upstream of the DMA-CPC and the AAC-CPC arrangements and the sampled particles were either passed through or around the CS to obtain the size distribution of stripped versus non-stripped particles. Size distributions of stripped particles were corrected for the particle losses due to diffusion and thermophoresis in the CS based on penetration data provided by the manufacturer (Catalytic Instruments, Application Note CI-0009) as follows

$$P = 0.670 \left(0.190 e^{-\frac{499}{d_p^2}} + 0.925 e^{-\frac{36}{d_p^2}} \right) \quad (20)$$

where d_p is the geometric diameter of the particle (in nm). The penetration efficiency of the CS at 350 °C has also been measured by Woo et al. (2021), which shows good agreement with

manufacturer's penetration function (see the Supplementary Material). Both data sets show a relatively constant penetration (~ 0.7) for particles larger than 30 nm and a sharp decrease in penetration for particles smaller than 20 nm.

Similar to volatile mass fraction, we can determine the volatile number fraction of particles, $f_{n,v}$, from the number of non-stripped particles at each mobility diameter, $n_{ns}(d_m)$, and the number of stripped particles with the same mobility diameter, $n_s(d_m)$, as follows

$$f_{n,v} = 1 - \frac{n_s(d_m)}{n_{ns}(d_m)}. \quad (21)$$

The volatile number fraction is a measure of external volatility because it represents the number fraction of completely semi-volatile particles which evaporate and oxidize in the heated CS and have no non-volatile core. Note that the number of stripped particles were corrected for particle losses in the CS when using Eq. (21).

Arrangement C (Figure 1) was used to collect samples for off-line chemical and morphological analyses. Polydisperse particles were collected on quartz-fiber filters (Pall Corp., Model TissuQuartz 2500QAT-UP) using a home-built double-filter sampler, which also separated and collected the gas-phase semi-volatiles (Ngo et al., 2020). Size-selected particles by aerodynamic diameter were collected on aluminum foils with a micro-orifice uniform-deposit impactor for nanoparticles (Nano-MOUDI II; TSI Inc., Model 125R). To investigate the morphology of the particles by transmission electron microscopy (TEM), the Nano-MOUDI was also modified to accommodate lacey carbon film on 200 mesh copper TEM grids (Agar Scientific, Model AGS166H). Additionally, a combination of a nano-DMA (TSI Inc., Model 3085) and a nanometer aerosol sampler (NAS; TSI Inc., Model 3089) was used to collect size-selected particles by mobility diameter on silicon nitride (SiN) TEM grids (Norcada, Model NT050Z) for morphological characterization. The SiN grids were 3.0 mm in diameter with 10-nm thick nitride windows (0.5×0.5 mm in size) on a 200- μ m thick silicon frame. Sample collection time was 20 min for Nano-MOUDI with a flow rate of 10 L/min and 30–45

min for DMA-NAS setup with a flow rate of 1 L/min. We expect the particle collection efficiency to be low as the stated collection times resulted in relatively low number of particles deposited. The CS was used upstream of the Nano-MOUDI, the DMA-NAS, and the double-filter sampler to collect stripped versus non-stripped particles. TEM images of the collected particles were obtained using a transmission electron microscope (FEI, Model Tecnai G2-20 Twin) operating at an accelerating voltage of 200 kV.

4. Results and Discussion

4.1. Particle size distributions

Figure 3(a) shows representative mobility diameter and aerodynamic diameter size distributions measured by DMA-CPC and AAC-CPC, respectively, for non-stripped and stripped particles. The particles were sampled at engine speed of 2000 rpm and 6 bar load. The size distributions of stripped particles were corrected for particle losses in the CS (as discussed in Section 3) and Figure 3(a) also shows the uncorrected mobility diameter size distribution for comparison. It should be noted that the particle size distributions shown here are not corrected for dilution ratio, although the dilution was kept constant (*i.e.* 30:1) for all tests (see Section 3). The right tail of the mobility diameter size distributions shown in dashed line was projected where measured data were unavailable ($> \sim 150$ nm) by using an equation of two lognormal distributions that was fit to the measured data. As will be shown in Section 4.2, the projected part will become important when determining the mass distribution and mixing state of particles.

The particle size distributions show that the total number concentration of non-stripped and stripped particles was $2.2 \times 10^5 \text{ cm}^{-3}$ and $1.3 \times 10^5 \text{ cm}^{-3}$, respectively (in the case of aerodynamic diameter size distribution). This result highlights a significant decrease ($\sim 40\%$) in the number concentration of particles due to catalytic stripping. This observation indicates a large fraction of semi-volatile particles in the aerosol population, which were removed

(evaporated and oxidized) subsequent to being passed through the catalytic stripper. Although the size distribution of stripped particles was corrected for particle losses in the CS, this decrease in particle concentration may, to some extent, be due to higher diffusion losses as a result of particles becoming smaller in size after passing through the catalytic stripper. The existence of a large fraction of semi-volatile particles was confirmed by TEM images as well as off-line chemical analysis (see Section 4.8). Figure 3(b) shows representative TEM images of non-stripped particles collected using the DMA-NAS arrangement. As can be seen in these images, a large number of spherical particles existed in non-stripped condition; however, most of these particles disappeared when the sample was passed through the CS. This indicates that the spherical particles are semi-volatile which condense as liquid droplets at ambient temperature.

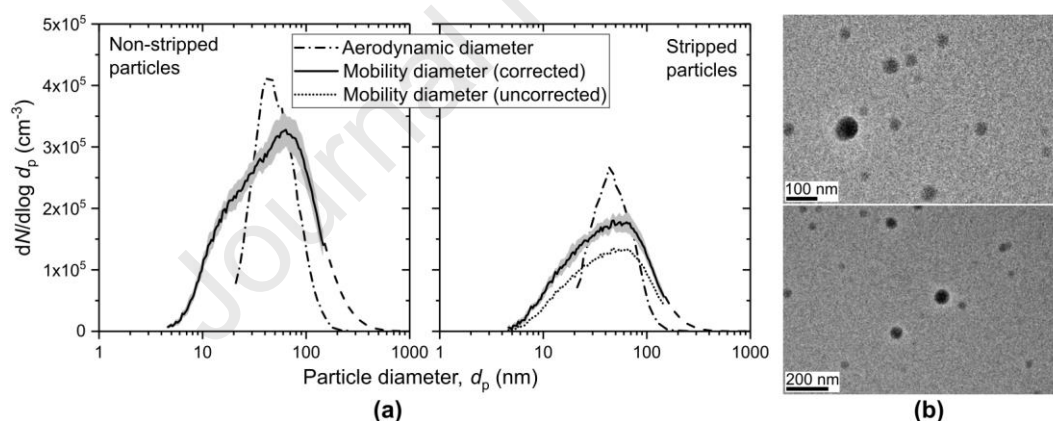


Figure 3: (a) Representative mobility and aerodynamic diameter size distributions for non-stripped and stripped particles sampled from the engine operating at 2000 rpm and 6 bar. The grey band shows the precision uncertainty for the mobility diameter size distribution based on several repeated measurements. The solid lines show measured data and the dashed lines show the projection (extrapolation) based on measured data. The particle size distributions are corrected for particle losses in the CS and bypass line; however, the dotted line shows the uncorrected mobility diameter size distribution for comparison. (b) TEM images of non-stripped particles, showing a large number of the spherical semi-volatile particles which disappeared when the sample was passed through the CS. The average diameter of these particles was 43.2 ± 14.2 nm using ImageJ software.

Figure 3(a) also shows that the aerodynamic diameter size distributions generally have lower geometric standard deviations (GSD) compared to the mobility diameter size distributions. For example, the GSD of the aerodynamic diameter and mobility diameter size

distributions of non-stripped particles was ~ 1.6 and ~ 2.1 , respectively. This observation can be explained by the fact that particles with different masses can have the same aerodynamic diameter and can be classified in the same size bin. The effective density of aggregate particles, such as soot, often decreases as the particle size increases (Olfert & Rogak, 2019). Thus, smaller particles with lower mass and drag force can have the same relaxation time (and aerodynamic diameter), but different mobility, as larger particles with higher mass and drag force (Johnson et al., 2021). This results in a narrower aerodynamic diameter size distribution for non-spherical particles, as particles at one aerodynamic diameter had a range of mobility diameters.

The mobility diameter size distributions for both stripped and non-stripped particles were not lognormal distributions and showed negative skewness, which appeared as right-leaning distributions. The non-lognormal distribution measured in the current study has been reported in several previous measurements of PM emissions from GDI engines (Graves et al., 2017; Gu et al., 2012; Momenimovahed & Olfert, 2015; Zhang et al., 2014). In contrast, the aerodynamic diameter size distributions of stripped and non-stripped particles appeared as symmetric lognormal distributions. If two species with different densities are present in the non-stripped particles, the aerodynamic diameter size distribution is expected to be bimodal; however, this was not seen in this study. As noted earlier in Section 3 and will be discussed in details in Sections 4.3 and 4.5, the effective density of soot particles are close to the density of semi-volatile particles in this study. Thus, the two species have similar aerodynamic diameters and are correctly characterized by the AAC as a single mode in the aerodynamic diameter size distribution. The median aerodynamic diameter of particles did not change significantly due to stripping and was ~ 45 nm for both non-stripped and stripped particles. Due to skewed mobility diameter size distributions, the mode diameter (peak) of these distributions are compared rather than their median diameter. The mode diameter of the mobility diameter size distribution for

both non-stripped and stripped particles was ~60–65 nm. Consistent with our measurements, Graves et al. (2017) and Momenimovahed and Olfert (2015) have also reported an average median mobility diameter in the range of ~55–65 nm for PM emissions from GDI engines depending on the engine load.

4.2. Particle mixing state

Mixing state determines the fraction of externally mixed particles (*i.e.* when purely semi-volatile particles exist separate from non-volatile particles) and internally mixed particles (*i.e.* when semi-volatile species exist as adsorbed coating on the surface of non-volatile particles). The particle size distribution, volatile number fraction, and volatile mass fraction can be used to determine the mass distribution and mixing state of non-stripped particles. Previous studies (Dickau et al., 2016) have contributed in methods to quantify the mixing state of the aerosols when non-volatile and semi-volatile particle species coexist. In this study, we have evidences of both externally- and internally-mixed semi-volatile particles with non-volatile particles. As showed in Section 4.1, the number of stripped particles decreased significantly compared to non-stripped particles, which indicates the existence of purely semi-volatile particles that are externally mixed with non-volatile particles. Moreover, Figure 2 shows that the average mass of size-selected particles decreased when passed through the CS (from 0.067 to 0.057 fg for particles with $d_m=50$ nm), indicating the existence of adsorbed semi-volatile coating on non-volatile particles. Here, we follow the method of Dickau et al. (2016), which will be described briefly below, to determine the mixing state of non-stripped particles. Note that precise quantification of the mixing state must account for particle losses (*e.g.* due to diffusion and thermophoresis) in the catalytic stripper such that volatile number fraction is determined accurately.

The mass distribution of purely semi-volatile particles (externally mixed) can be obtained as follows

$$\frac{dM_{pv}}{d \log d_m} = m_{pv}(d_m) f_{n,v}(d_m) \frac{dN}{d \log d_m} = \left(\frac{\pi}{6} d_m^3 \rho_{pv} \right) f_{n,v}(d_m) \frac{dN}{d \log d_m} \quad (22)$$

where m_{pv} is the mass of a purely semi-volatile particle, $f_{n,v}$ is the volatile number fraction from Eq. (21), and $dN/d \log d_m$ is the mobility diameter size distribution of non-stripped particles shown in Section 4.1. Note that these quantities are a function of mobility diameter. The mass of purely semi-volatile particles was obtained by assuming a spherical particle with the density of semi-volatile species, ρ_{pv} . The material density of semi-volatile species was assumed to be $1000 \pm 250 \text{ kg/m}^3$ as will be discussed in details in Section 4.5.

The mass distributions of adsorbed semi-volatile particles (internally mixed) and non-volatile particles can be obtained from

$$\frac{dM_{ad}}{d \log d_m} = m_{ns}(d_m) f_{m,v}(d_m) \left(1 - f_{n,v}(d_m) \right) \frac{dN}{d \log d_m} \quad (23)$$

$$\frac{dM_{nv}}{d \log d_m} = m_{ns}(d_m) \left(1 - f_{m,v}(d_m) \right) \left(1 - f_{n,v}(d_m) \right) \frac{dN}{d \log d_m} \quad (24)$$

where m_{ns} is the mass of a non-stripped particle and $f_{m,v}$ is the volatile mass fraction from Eq. (19). Again, these quantities are a function of mobility diameter. We will determine the relationships for the mass of non-stripped particles and the volatile mass fraction as a function of mobility diameter in Sections 4.3 and 4.7, respectively, and we have used these relationships for the results presented in this section.

Once the mass distribution of each particle species is determined as described above, the total mass of each component (externally- or internally-mixed semi-volatiles and non-volatile particles) can be found by integrating their corresponding mass distribution. Moreover, the total mass of semi-volatile species (regardless of their mixing state) and non-volatile species can be determined as follows:

$$M_{\text{volatile}} = \sum \left(\frac{dM_{pv}}{d \log d_m} + \frac{dM_{ad}}{d \log d_m} \right) d \log d_m \quad (25)$$

$$M_{\text{nv}} = \sum \left(\frac{dM_{\text{nv}}}{d \log d_m} \right) d \log d_m \quad (26)$$

We will use the total mass of semi-volatile and non-volatile species later in Section 4.5 to determine the average density of non-stripped particles.

Figure 4(a) shows the mass distribution of purely semi-volatile (externally mixed), adsorbed semi-volatile (internally mixed), and non-volatile species for the non-stripped particles shown in Figure 3. The solid lines in the mass distributions correspond to the measured data (up to ~150 nm) and the dashed lines correspond to where measured data were unavailable (*i.e.* the projected part of the mobility diameter size distribution in Figure 3). This projected part was drawn to represent the mass distribution without missing a portion of the mass found at larger particles. It can be seen that the measured particle size distribution can only capture a section of the mass distribution for purely semi-volatile and non-volatile species. Nonetheless, it is still useful to investigate the mixing state of each species by comparing their total mass fraction based on measured and projected sections. It is apparent that mass distributions have shifted to the right compared to the size distributions because a greater proportion of mass is in the larger particles. The median mass diameter of purely semi-volatile, adsorbed semi-volatile, and non-volatile particles is at ~180, ~80, and ~245 nm, respectively. Moreover, purely semi-volatile particles had the most significant mass distribution, followed by non-volatile particles. The mass distribution of adsorbed semi-volatile species was by far the least significant compared to the other two.

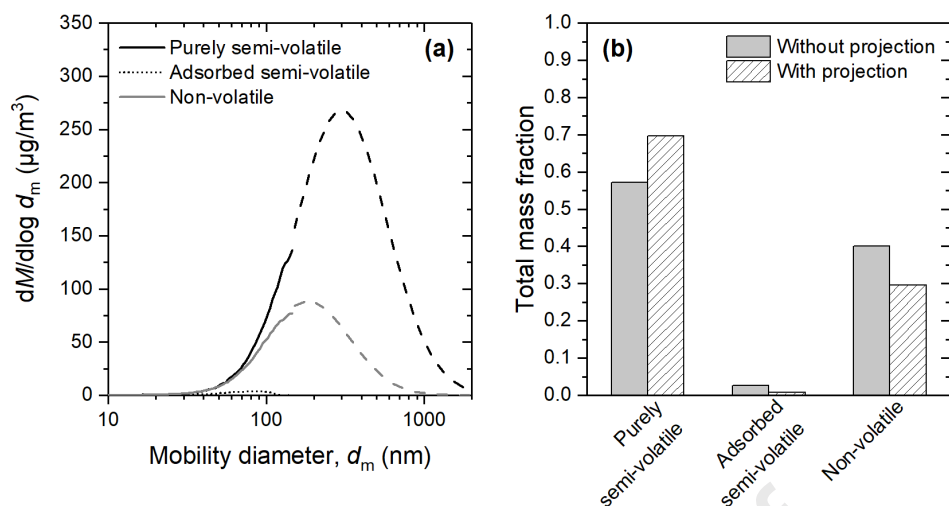


Figure 4: (a) Mass distribution of purely semi-volatile particles (externally mixed), adsorbed semi-volatiles (internally mixed), and non-volatile particles existing in the non-stripped particles sampled from the engine operating at 2000 rpm and 6 bar. The solid and dashed lines represent the measured and projected parts of the mass distributions. (b) The total mass fraction of purely semi-volatile particles, adsorbed semi-volatiles, and non-volatile particles with and without considering the projected part of the mass distributions.

Figure 4(b) shows the total mass fraction of externally- or internally-mixed semi-volatile particles as well as non-volatile particles for the non-stripped particles shown in Figure 3. These results reveal that by considering the measured data only (without projection), approximately 57.3%, 40%, and 2.7% of the total mass was due to purely semi-volatile, non-volatile, and adsorbed semi-volatile particles, respectively. When considering the projected mass distributions, approximately 69.7%, 29.6%, and 0.7% of the total mass was due to purely semi-volatile, non-volatile, and adsorbed semi-volatile particles, respectively. In either case, it is clear that the externally mixed semi-volatile particles were the dominant species in terms of mass, followed by non-volatile particles. The internally mixed semi-volatile coating on soot particles accounted for a very small fraction of the total mass. These results also show that extrapolating the measured data did not drastically change the total mass fraction of each component (*e.g.*, the total mass fraction of semi-volatiles changed from ~60% to ~70% when considering projection). These results are quite different from previous studies that have determined the mixing state of particles following a similar method. For example, Graves et al. (2017) reported total mass fraction of semi-volatiles of 10% and 6.8% for a GDI engine

operating at torques of 45 and 90 N·m, respectively. This difference is plausibly because a catalytic converter was used at the exhaust manifold of their engine, which oxidized the majority of the mass of unburned hydrocarbons into CO₂ and water. This explanation is generally consistent with Storey et al. (2010) who reported a significantly higher mass of organic carbon compared to elemental carbon (ratios of 2–5) for pre-catalyst samples using thermal-optical method. Unlike Graves et al. (2017), we did not use a catalytic converter in our study and thus a greater mass of unburned hydrocarbons was present in the exhaust, which could form externally- or internally-mixed semi-volatiles in cooled and diluted state.

4.3. Mass-mobility and effective density of polydisperse particles

Figure 5(a) shows a representative mass-mobility relationship for polydisperse particle emissions at engine speed of 1200 rpm and load of 6 bar using the DMA-CPMA arrangement. The mass-mobility relationship for other engine operating conditions is shown in the Supplementary Material. The error bars represent the total uncertainty in particle mass based on propagation of precision and bias uncertainties (see the Supplementary Material for details). The mass of mobility-selected particles was measured and a power-law fit was used as follows to correlate mass and mobility diameter of particles:

$$m = kd_m^{D_m} \quad (27)$$

where k is the pre-factor of the fit and D_m is the mass-mobility exponent. For spherical particles $D_m = 3$ and for non-spherical particles $D_m < 3$. Olfert and Rogak (2019) have shown that fresh soot aggregates with lacy structure from various combustion sources—such as compression and spark ignition engines, gas turbines, and a wide range of diffusion and premixed flames—have an average $D_m \sim 2.5$.

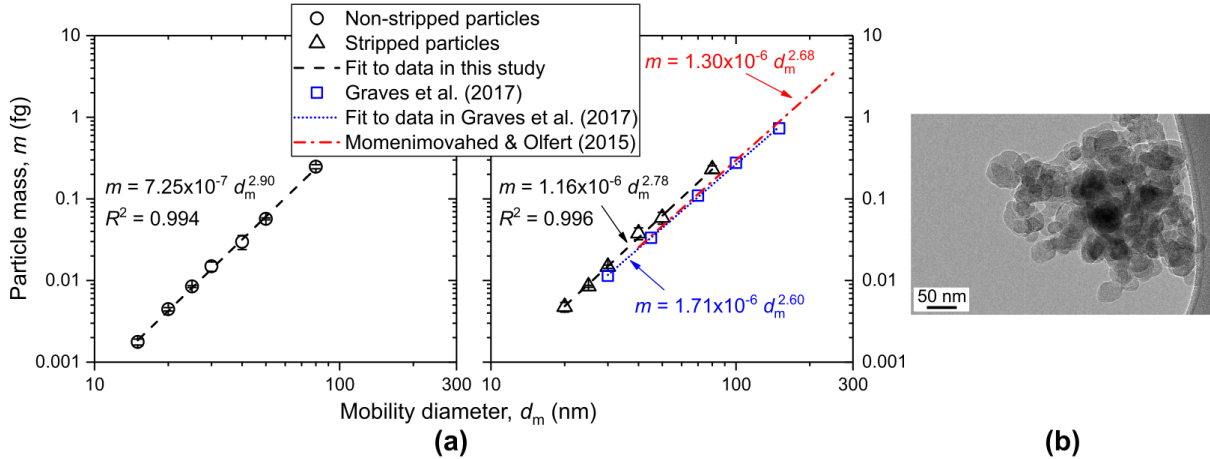


Figure 5: (a) Mass-mobility relationship of polydisperse non-stripped and stripped particles at engine speed of 1200 rpm and load of 6 bar. The error bars represent the total uncertainty in particle mass. (b) Representative TEM image of stripped particles, which show that the particles had a compact structure.

As shown in the left panel of Figure 5(a), the mass-mobility exponent of non-stripped particles was 2.90. One explanation for this observation is the existence of a large number of spherical semi-volatile droplets (with $D_m = 3$) in the aerosol population (as discussed in Section 4.1 and shown in the TEM images in Figure 3(b)) alongside the population of non-spherical soot particles (with $D_m = 2.78$, as discussed below). Thus, it is reasonable to expect an intermediate value of $D_m = 2.90$ (which falls between 2.78 and 3) for the non-stripped particles. Similar to this observation, Graves et al. (2015) also reported $D_m = 3.0$ for undenuded particles from a natural gas high-pressure direct-injection (HPDI) engine at a low-load operating condition which generated a large number fraction ($\sim 45\%$) of externally-mixed semi-volatile particles (25% of maximum load at 1500 rpm).

As shown in the right panel of Figure 5(a), the mass-mobility exponent of stripped particles was 2.78. This implies that the soot particles without any semi-volatile coating had a compact structure, which is also confirmed by the TEM images shown in Figure 5(b). The compact structure of stripped particles could be due to the restructuring of soot aggregates in the engine exhaust as a result of the surface tension of semi-volatile coating, which can potentially collapse the lacy structure of the soot aggregate. The volatile mass fraction is a measure of internal mixing of semi-volatile species with soot aggregates; thus, a higher volatile mass

fraction can result in a greater degree of restructuring (Ghazi & Olfert, 2013). Presumably, externally mixed semi-volatile particles have little effect on restructuring of soot aggregates, unless both species become internally mixed. Previous studies in the literature have reported the restructuring of flame and engine soot aggregates into compact clusters due to condensation of a variety of volatile material such as secondary organic aerosol (Leung et al., 2017; Schnitzler et al., 2014), oleic acid (Bambha et al., 2013; Ghazi & Olfert, 2013; Slowik, Cross, Han, Kolucki, et al., 2007), and sulfuric acid (Pagels et al., 2009). These studies collectively reported an increase in the D_m of soot aggregates after coating and denuding process due to the restructuring of soot into a compact form. For example, Schnitzler et al. (2014) reported that the mass-mobility exponent of flame soot particles changed from 2.24 to 2.78 (*i.e.* from lacy to compact structure) as a result of restructuring due to the condensation of secondary organic aerosols on soot particles. Graves et al. (2015) also reported the collapse (or restructuring) of soot aggregates from an HPDI engine in conditions with high volatile mass fraction. Note that the volatile mass fraction of a particle, $f_{m,v}$, which will be discussed in section 4.7, should not be confused with the total mass fraction of adsorbed semi-volatiles obtained in section 4.2; the latter indicates the extent of internal versus external mixing of semi-volatiles for the aerosol population and not for a single particle.

It is noteworthy that the D_m of polydisperse particles reported here is slightly higher compared to previous studies on GDI engines, as shown in the right panel of Figure 5(a), due to the reasons explained earlier and below. Momenimovahed and Olfert (2015) reported a D_m in the range of ~ 2.6 – 2.74 for non-volatile (denuded) particles from four vehicles with GDI engines, showing that D_m values as high as ~ 2.75 are not uncommon. These authors used a chassis dynamometer to run the 4-cylinder engines with commercial gasoline at a torque of 19 N·m (6.1 kW) and 38 N·m (12.2 kW) at steady-state condition at a speed of 60 km/h. Graves et al. (2017) also reported an average D_m of 2.6 for denuded particles from a GDI engine at a

torque of 90 N·m (133 kW). These authors used a dynamometer to run the 4-cylinder engine with commercial ethanol-free gasoline and injection timing of 280° before top dead center. The engine exhaust was fitted with a catalytic converter, which oxidized and removed the majority of unburned hydrocarbons from the fuel or lubricant oil. In Momenimovahed and Olfert (2015), Graves et al. (2015), and the current study, the volatile mass fraction of soot particles from the engine exhaust was high because a catalytic converter was not used to remove the semi-volatile species. Thus, the soot aggregates underwent a greater degree of restructuring in these studies, which resulted in structures that are more compact with higher mass-mobility exponent. On the other hand, Graves et al. (2017) reported a very low volatile mass fraction (< 5% for all particle sizes), which could be due to the use of a catalytic converter in their study. Thus, the soot particles underwent little restructuring due to semi-volatile coatings and the reported mass-mobility exponents were lower. The results of these studies and the current study collectively and consistently indicate that whenever the volatile mass fraction of engine PM emissions is high, there is a greater degree of soot restructuring leading to a higher value for D_m . In addition to the restructuring of soot, the slightly higher D_m for polydisperse particles in this study could also be due to the smaller range of particle mobility diameters used in the mass-mobility measurements. The smaller range of particles produced by the GDI engine in this study limited the mass-mobility measurements to mobility diameters less than ~100 nm (see Section 3), consistent with other studies which show that soot particles from GDI engines are predominantly smaller than 100 nm (Di Iorio et al., 2021; X. Wang et al., 2016). To show the latter explanation, when the mass-mobility data reported in Graves et al. (2017) is limited to mobility diameters less than 100 nm, the D_m increases from 2.6 to 2.67, implying that the range of particles considered may influence reported D_m values.³

³ The least-square fitting procedure commonly used to obtain the mass-mobility relationship uses greater weight for data points with higher values (*e.g.* larger particles with higher mass), which results in lower D_m values close to that of larger aggregates with less compact structure.

Combining Eq. (16) and (27), the particle effective density can be expressed as

$$\rho_{\text{eff}} = \frac{6k}{\pi} d_m^{D_m-3} \quad (28)$$

For spherical particles, $D_m = 3$ and the effective density is constant, while for non-spherical particles, $D_m < 3$ and the effective density decreases as the mobility diameter increases. Figure 6 shows the effective density of the non-stripped and stripped polydisperse particles shown in Figure 5(a). The error bars represent the total uncertainty in particle effective density based on DMA-CPMA measurements. The effective density of polydisperse particles for other engine operating conditions is shown in the Supplementary Material. The effective density of non-stripped particles was relatively constant in the range of $\sim 875 - \sim 1050 \text{ kg/m}^3$ (with an average of 975 kg/m^3) in the mobility range of 15–80 nm, which showed that these particles were nearly spherical—a result also confirmed by the TEM images in Figure 3(b). The range of effective density values for non-stripped particles were close to the material density of semi-volatile organic compounds ($\sim 780 - \sim 1250 \text{ kg/m}^3$ as will be shown in Section 4.5), showing the existence of a large fraction of semi-volatile particles.

On the other hand, the effective density of stripped particles decreased slightly from ~ 1150 to $\sim 850 \text{ kg/m}^3$ as their mobility diameter increased from 20 to 80 nm. Previous studies (such as Graves et al., 2017) have reported a lower effective density for denuded soot particles from GDI engines (*i.e.*, from ~ 800 to $\sim 550 \text{ kg/m}^3$ for a mobility range of 30–80 nm). The higher effective density and its lower sensitivity to particle size indicate that soot particles in our study had a relatively more compact structure. The void space between primary particles is less in a compact aggregate compared to an aggregate with branched and open structure, leading to higher effective density (due to smaller particle volume). As noted earlier, the compact stripped particles in our study were plausibly due to a higher degree of aggregate restructuring as a result of higher semi-volatile coating on soot particles or because of the smaller range of particle mobility diameters. Consistent with our results here, Graves et al. (2015) also reported

denuded particles with higher effective density values and higher D_m in HPDI engine modes with high volatile mass fraction. Previous studies that reported lower effective densities for GDI engine soot and stronger dependence on particle size (such as Graves et al., 2017) had a much lower mass fraction of semi-volatile coating on soot particles (< 5%) compared to our study. Thus, in those studies the soot particles underwent a much lower degree of restructuring as a result of mixing with volatile material, resulting in branched aggregates with lower effective densities.

It is also worthwhile to compare the effective density of stripped particles with the universal fit of Olfert and Rogak (2019) and we have included this fit and its variation (shaded area) in the right panel of Figure 6. Evidently, the decreasing trend in the effective density of stripped particles (from 1150 to 850 kg/m³) is in agreement with the study of Olfert and Rogak (2019) for non-volatile soot aggregates in the size range of 20–80 nm and within its reported variation. However, they reported a steeper decrease in effective density with increasing mobility diameter up to ~400 nm. This stronger size dependence is presumably due to the large number of low-volatility test conditions included in the study of Olfert and Rogak (2019), which resulted in less restructuring of soot particles into compact clusters. The substantial scatter (~20% variation) around the universal effective density fit by Olfert and Rogak (2019) is due to a wide range of combustion sources used in their study, including compression ignition and spark ignition engines, gas turbines, and a range of premixed and non-premixed burners. These authors reported that some internal combustion engines produce soot with higher effective density (consistent with our results), while gas-turbine soot tends to have lower effective density.

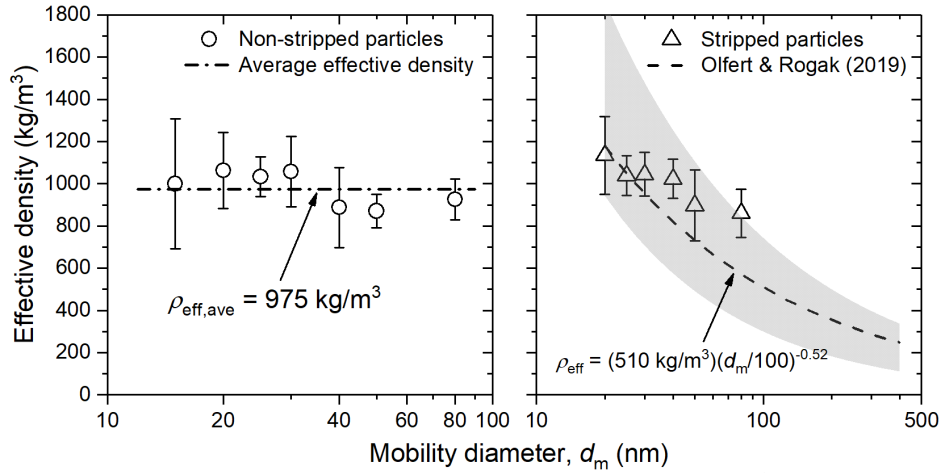


Figure 6: Representative effective density of non-stripped and stripped particles at engine speed of 1200 rpm and load of 6 bar. The error bars represent the total uncertainty in the effective density based on the DMA-CPMA method. The shaded area shows the scattered variation around the universal fit of Olfert and Rogak (2019).

4.4. Effective density of monodisperse particles

The effective density of monodisperse particles were determined by using the AAC-DMA-CPMA arrangement as described in Section 3. Briefly, particles of a certain aerodynamic diameter (*e.g.*, $d_a = 60 \text{ nm}$) were selected by the AAC, which were further classified for a certain mobility diameter (*e.g.*, $d_m = 55, 60, \text{ or } 65 \text{ nm}$) by the DMA and the mass of these monodisperse particles was measured by the CPMA. The effective density of the monodisperse particles was determined by three methods: the DMA-CPMA (Eq. (16)), the AAC-DMA (Eq. (17)), and the AAC-CPMA (Eq. (18)). The effective density of stripped particles was measured by passing the monodisperse particles through the CS upstream of the CPMA, as shown in Figure 1.

Figure 7 shows the effective density of non-stripped and stripped monodisperse particles by the three methods when their aerodynamic and mobility diameters were equal ($d_a = d_m$). The particles were sampled from engine operating condition of 1200 rpm and 12 bar. It is evident that the particle effective density values determined from the DMA-CPMA and the AAC-DMA methods were in good agreement ($< 15\%$ difference) and within the uncertainty of the measurements, for both non-stripped and stripped particles. However, the effective density of stripped particles obtained from the AAC-CPMA method had larger discrepancy (up

to 49% difference) with the other two methods. In contrast, the effective density of non-stripped particles from AAC-CPMA method agreed fairly well with the other two methods ($< 25\%$ difference, except for $d_m = 40$ nm), although with larger uncertainty.

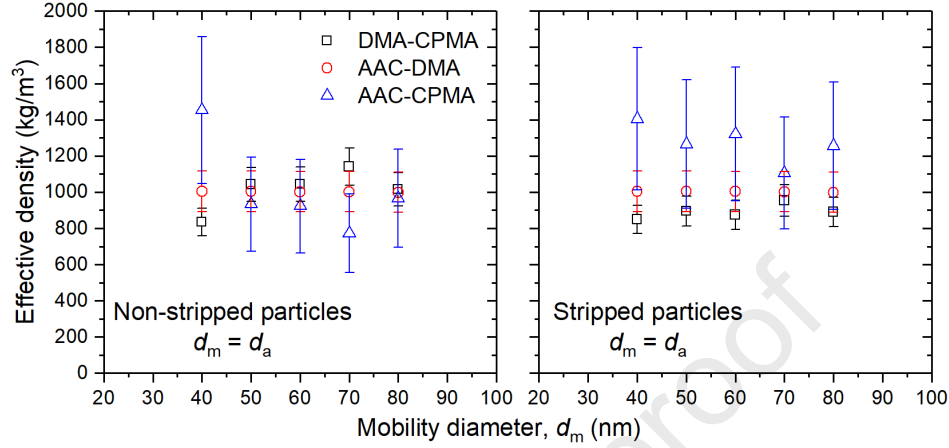


Figure 7: Effective density of monodisperse particles selected based on their aerodynamic and mobility diameters when $d_a = d_m$ using the DMA-CPMA, the AAC-DMA, and the AAC-CPMA methods for non-stripped and stripped conditions. The error bars represent the bias uncertainty of each corresponding method. The particles were sampled from the engine running at 1200 rpm and 12 bar.

A plausible explanation for these observations is the fact that classification by AAC does not constrain the properties of non-spherical particles (such as mass) as monodisperse as DMA or CPMA classification. Stripped particles are non-spherical and small and large particles with different masses can have the same relaxation time, as noted earlier in Section 4.1. Thus, particles of different mass can be classified by the AAC as having identical aerodynamic diameter. As a result, the effective density obtained from the AAC-CPMA method (having different mass in Eq. (18)) can deviate from the other two methods. In contrast, non-stripped particles are nearly spherical and classification by AAC results in particles with monodisperse mass, leading to effective density from AAC-CPMA method being in fair agreement with the other two methods. The large error bars of the effective density data based on AAC-CPMA method stem from Eq. (18), which uses mass to the power of 2 and aerodynamic diameter to the power of 6. As discussed in the Supplementary Material, propagation of uncertainty reveals that a small error in aerodynamic diameter can lead to a significant error in effective density—a 28.4% uncertainty in the effective density from AAC-

CPMA method compared to 9.4% and 11.1% uncertainties for DMA-CPMA and AAC-DMA methods, respectively. Similar to the results found here, Yao et al. (2020) reported that the effective density of ammonium sulfate particles in the mobility diameter range of 150–550 nm obtained from AAC-APM measurement was higher than the bulk density of the material, which was not physically reasonable, and had a higher uncertainty compared to DMA-APM and AAC-DMA methods.

The results in Figure 7 also shows that the effective density of non-stripped and stripped monodisperse particles from 40 to 80 nm, measured by the DMA-CPMA and the AAC-DMA methods, was nearly constant in the range of 800–1200 kg/m³. This result indicates that the monodisperse particles had very compact structure in this mobility diameter range, regardless of their volatility.

Figure 8 shows the effective density of non-stripped and stripped monodisperse particles by the three methods when their aerodynamic and mobility diameters were not equal ($d_a \neq d_m$). It is evident that the effective density of non-stripped and stripped particles determined based on the DMA-CPMA, the AAC-DMA, and the AAC-CPMA methods generally agreed with each other within the uncertainty of the measurements. However, the effective density of particles with $d_m = 35$ nm and $d_a = 40$ nm showed large deviations between the AAC-CPMA and the other two methods. Notably, the effective density of the stripped 35-nm particles obtained from the AAC-CPMA method was higher than the material density of soot and not physically reasonable, consistent with the findings of Yao et al. (2020) for ammonium sulfate particles.

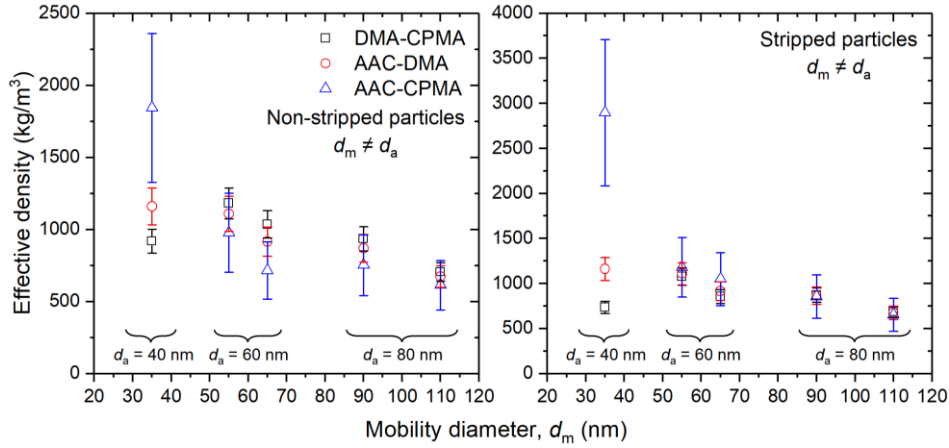


Figure 8: Effective density of monodisperse particles selected based on their aerodynamic and mobility diameters when $d_a \neq d_m$ using the DMA-CPMA, the AAC-DMA, and the AAC-CPMA methods for non-stripped and stripped conditions. Mobility diameter of 35 nm corresponds to particles with $d_a = 40$ nm, mobility diameters of 55 and 65 nm correspond to particles with $d_a = 60$ nm, and mobility diameters of 90 and 110 nm correspond to particles with $d_a = 80$ nm. The error bars represent the bias uncertainty of each corresponding method. The particles were sampled from the engine running at 1200 rpm and 12 bar.

4.5. Volume equivalent diameter of particles

Volume equivalent diameter of monodisperse particles selected by their aerodynamic and mobility diameter was determined based on the CPMA method (Eq. (6)) and the AAC-DMA method (Eq. (8)). In doing so, the material density of stripped particles was considered to be 1770 ± 70 kg/m³ reported for preheated diesel soot (Park et al., 2004). This material density is in agreement with the reported value of 1834 ± 187 kg/m³ for the true density of soot with less than 5% organic carbon content from diffusion flames with various gaseous and liquid fuels (Ouf et al., 2019). Non-stripped particles consisted of semi-volatile species that were mostly externally and far less internally mixed with non-volatile solid particles (see Section 4.2). The mean material density of non-stripped particles can be calculated as the total mass of semi-volatile and non-volatile species divided by the total volume of these species as follows (Slowik, Cross, Han, Davidovits, et al., 2007)

$$\rho_{\text{ns}} = \frac{M_v + M_{\text{nv}}}{V_v + V_{\text{nv}}} = \frac{M_v + M_{\text{nv}}}{\frac{M_v}{\rho_v} + \frac{M_{\text{nv}}}{\rho_{\text{nv}}}} \quad (29)$$

where M , V , and ρ are the total mass, total volume, and material density, respectively, and subscripts “v” and “nv” denote semi-volatile and non-volatile species, respectively. The total

mass of semi-volatile species consisted of purely semi-volatile particles and adsorbed semi-volatile coating and can be determined by using Eq. (25), while the total mass of non-volatile species can be determined by using Eq. (26).

Semi-volatile particles can have extremely complex chemical composition, containing many different organic compounds, such as *n*- and branched alkanes, *n*- and branched alkenes, aromatic hydrocarbons, saturated and unsaturated cycloalkanes, aliphatic and olefinic aldehydes, aromatic ketones, aromatic aldehydes, *n*-alkanoic acids, and many other oxygenated and paraffinic compounds (Funkenbusch et al., 1979; Schauer et al., 1999). A survey of these organic compounds show that their material density is in the range of $\sim 780 - \sim 1250 \text{ kg/m}^3$. Here, we assume an average material density of $1000 \pm 250 \text{ kg/m}^3$ for semi-volatile species, which covers the range observed in our survey. Thus, by using Eq. (29) the data presented in Section 4.2, we can estimate the mean material density of non-stripped particles as $\sim 1150 \text{ kg/m}^3$. Similarly, by considering the lower and upper limits in the material densities of semi-volatile and non-volatile particles, we estimate that the mean material density of non-stripped particles has a minimum and maximum value of ~ 940 and $\sim 1360 \text{ kg/m}^3$, respectively (note that the material density limits for semi-volatile and non-volatile species also affect their corresponding total mass). Thus, the mean material density of non-stripped particles was estimated to be $1150 \pm 210 \text{ kg/m}^3$, which is in agreement with the reported value of $1285 \pm 217 \text{ kg/m}^3$ for mean true density of soot with high ($>20\%$) organic carbon content (Ouf et al., 2019).

Figure 9 shows the volume equivalent diameter of non-stripped and stripped particles versus their mobility diameter based on AAC-DMA and CPMA methods. The particles were sampled from engine operating condition of 1200 rpm and 12 bar. Firstly, it is clear that the AAC-DMA and the CPMA methods result in volume equivalent diameters that agree very well with each other. Moreover, the volume equivalent diameter was relatively similar for non-

stripped and stripped particles, but due to different reasons. The mean material density of non-stripped particles was affected by the density of semi-volatile material as mentioned earlier, resulting in a volume equivalent diameter that was ~ 0.92 of the mobility diameter ($d_{ve} \sim 0.92d_m$) when accounting for the mean material density of the semi-volatile and solid material. In contrast, the stripped particles had a lower effective density than the mean material density within the particle due to their non-spherical structure, resulting in a volume equivalent diameter that was ~ 0.8 of the mobility diameter ($d_{ve} \sim 0.8d_m$). Thus, it is expected that the stripped particles have a relatively compact structure, consistent with TEM images in Figure 5(b).

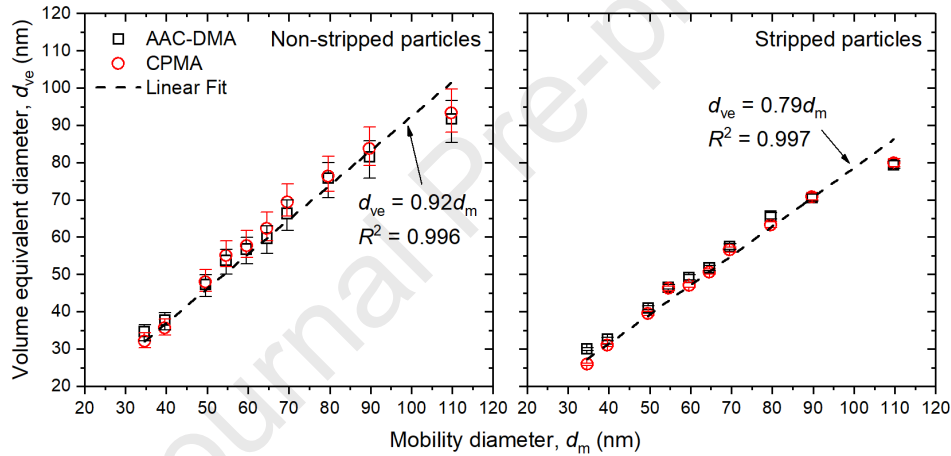


Figure 9: Volume equivalent diameter of non-stripped and stripped particles determined by the AAC-DMA and the CPMA methods. The particles were sampled from engine operating condition of 1200 rpm and 12 bar. The error bars represent the lower and upper limit of d_{ve} based on the minimum and maximum values estimated for material density of particles. Dashed lines are linear fits (with zero intercept) to the data points.

4.6. Dynamic shape factor of particles

Dynamic shape factor of monodisperse particles selected by their aerodynamic and mobility diameters was determined based on the AAC-CPMA method (Eq. (12)) and the DMA-CPMA method (Eq. (13) with the assumption that the particles are singly-charged). The volume equivalent diameter required in the AAC-CPMA and DMA-CPMA methods was calculated based on Eqs. (8) and (6), respectively, as discussed in Section 4.5. The material density required in Eq. (12) was considered to be 1770 ± 70 and 1150 ± 210 kg/m^3 for stripped and

non-stripped particles, respectively (similar to Section 4.5). The particles were sampled from engine operating condition of 1200 rpm and 12 bar. Figure 10 shows the dynamic shape factor of non-stripped and stripped particles versus their mobility diameter based on both methods. The error bars show the lower and upper limit of the dynamic shape factor based on the minimum and maximum values of material density and volume equivalent diameter, as discussed in Section 4.5. The large error bars in the shape factor of non-stripped particles using the AAC-CPMA method stem from the large uncertainty in their mean material density ($\sim 18\%$, see Section 4.5) and the fact that dynamic shape factor in Eq. (12) is directly proportional to the material density. The uncertainty in the material density of stripped particles was much smaller ($\sim 3.9\%$).

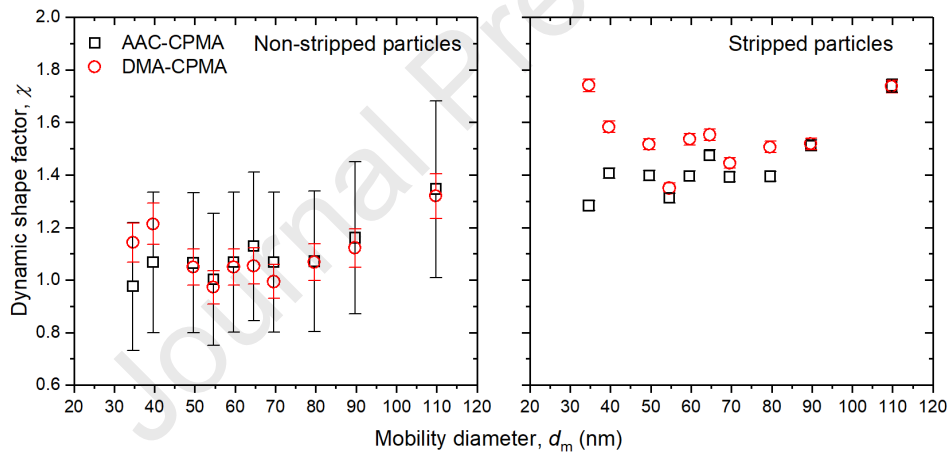


Figure 10: Dynamic shape factor of non-stripped and stripped particles (from engine operating condition of 1200 rpm and 12 bar) determined based on AAC-CPMA and DMA-CPMA methods. The error bars represent the lower and upper limit of the dynamic shape factor based on the minimum and maximum values of material density and volume equivalent diameter.

The dynamic shape factor obtained from the AAC-CPMA method generally increased as the mobility diameter increased for both non-stripped and stripped particles. Although the dynamic shape factor based on the DMA-CPMA method followed the same trend for particles with $d_m > 50$ nm, for smaller particles ($d_m < 50$ nm) the shape factor had a large value, which was not physically reasonable. Although the AAC-CPMA method had a much larger uncertainty, this method gives dynamic shape factors that are more physically reasonable

compared to those obtained from the DMA-CPMA method and we use the results of the former method for the rest of this study. Furthermore, the left panel in Figure 10 shows that the dynamic shape factor of non-stripped particles slightly increased from ~ 1.0 to ~ 1.3 as the mobility diameter increased from 35 to 110 nm. For spherical particles, the dynamic shape factor is equal to 1 ($\chi = 1$); however, non-spherical particles with lacy structure (such as soot particles) have a dynamic shape factor much greater than 1 ($\chi \gg 1$). Therefore, it is expected that small non-stripped particles with a dynamic shape factor in the narrow range of 1.0–1.1 were nearly spherical, consistent with TEM images shown in Figure 3(a) and the large fraction of purely semi-volatile particles in this case. Large non-stripped particles had a greater dynamic shape factor (~ 1.3), indicating these particles had a non-spherical but compact structure.

The right panel in Figure 10 shows that the dynamic shape factor of stripped particles was greater than that of non-stripped particles and gradually increased from ~ 1.3 to ~ 1.75 as the mobility diameter increased from 35 to 110 nm. The trend and range of dynamic shape factor observed here for stripped soot particles are in general agreement with previous reports in the literature. Tavakoli and Olfert (2014) reported that the dynamic shape factor of soot particles from an inverted-flame burner (with mass-mobility exponent of ~ 2.2) increased from ~ 1.5 to ~ 2.6 as the soot mobility diameter increased from 95 to 637 nm. Khalizov et al. (2012) also reported that the dynamic shape factor of soot particles from a fuel-rich propane premixed flame increased from 1.2 to 2.6 as the mobility diameter increased from 46 to 240 nm. The measurements in this study show that smaller stripped particles had compact aggregate structure (lower shape factor), whereas larger stripped particles had lacy aggregate structure (greater shape factor).

4.7. Volatile mass fraction of particles

Figure 11 shows the volatile mass fraction of particles, determined from Eq. (19), as a function of particle mobility diameter (left panel) and dynamic shape factor of particle (right panel). The

dynamic shape factors are those of the stripped particles based on the AAC-CPMA method, as described in Section 4.6. The particles were sampled from engine operating condition of 1200 rpm and 12 bar. It is evident from the left panel that the volatile mass fraction was higher for smaller particles and decreased consistently with the increase of particle mobility diameter. Semi-volatile compounds are found to be ~20% of total particle mass (non-volatile core and semi-volatile coating) for 30-nm diameter particles, while the volatile mass fraction was ~3% for 110-nm particles. The condensation of semi-volatile compounds on small particles changes their mass much faster than on large particles. A linear fit to the data is shown in the left panel of Figure 11 and is useful when deriving the mass distribution of adsorbed semi-volatile species and non-volatile particles using Eqs. (23) and (24) (refer to Section 4.2). The decreasing trend of volatile mass fraction with particle size is consistent with previous reports in the literature. Momenimovahed and Olfert (2015) reported that for vehicles with GDI engine tested on a dynamometer, the volatile mass fraction of particles was in the range of 10% to 30% for various engine powers and it decreased from ~25% for 60-nm particles to ~10% for 200-nm particles at engine power of 5%. They also reported that the higher the engine power, the greater the volatile mass fraction of particles at all particle mobility diameters. Other studies also showed a decreasing trend in volatile mass fraction of soot particle with its mobility diameter for particles emitted from diesel engines (Ristimäki et al., 2007; Sakurai et al., 2003), compression-ignition natural-gas direct-injection engine (Graves et al., 2015), and premixed ethylene flame (Ghazi et al., 2013).

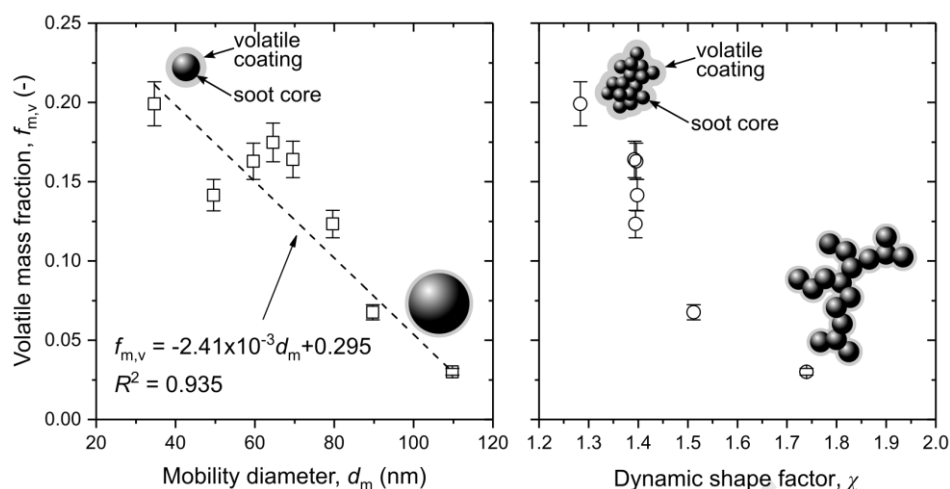


Figure 11: Volatile mass fraction as a function of particle mobility diameter (left panel) and particle dynamic shape factor (right panel). In the left panel, the mobility equivalent diameter of a particle is schematically shown as a black sphere and the semi-volatile coating in grey. In the right panel, a soot particle with lower shape factor (~ 1.3) is represented with a compact aggregate structure, while a soot particle with higher shape factor (~ 1.75) is represented with a lacy aggregate structure. The particles were sampled from engine operating condition of 1200 rpm and 12 bar. The error bars in the volatile mass fraction is based on the propagation of bias uncertainty in particle mass measured by the CPMA.

It is also clear from Figure 11 (right panel) that the volatile mass fraction of particles decreased as their dynamic shape factor increased from ~ 1.3 to ~ 1.75 . As it was previously shown in Figure 10(a), particles with smaller mobility diameter generally have a lower shape factor and we know from Figure 9 (left panel) that smaller particles have higher volatile mass fraction. Thus, it is expected that particles with lower shaper factor have a higher volatile mass fraction. The same explanation is also valid for larger particles with greater shape factor.

4.8. Chemical characterization of size-selected particles

The off-line chemical characterization of particles and gas phase sampled from the exhaust in parallel with the on-line measurements described above was performed using a two-step laser mass spectrometer (Duca et al., 2019; Faccinetto et al., 2015) and is presented in detail in a separate paper (Duca et al., 2021). Only the main findings of the latter study are briefly reminded here, as they are in very good agreement with the conclusions reached by the physical characterization performed in the present paper. Firstly, the study of size-selected non-stripped particles revealed an increasing contribution of organic compounds (associated with the volatile mass fraction) toward smaller particles sizes. This is illustrated in Figure 12 by a

volcano plot of particles collected in two size-bins (18–32 nm and 56–100 nm). Figure 12 clearly shows the predominant contribution of hydrocarbon species (associated with organic content) for the smaller particles, while bare carbon clusters (associated with elemental carbon content) have a significantly higher contribution to the mass spectra of larger particles. Furthermore, the analysis of stripped versus non-stripped size-selected particles revealed that the highest impact of the CS on the mass spectrometry signals related to surface adsorbed organics was observed for the smallest particles (10–18 nm and 18–32 nm size bins), *i.e.* these particles carry the highest volatile mass fraction (Duca et al., 2021). The CS impact on the mass spectrometry signals associated with the organic carbon content evolves for the larger particles in a way which matches the trend shown in Figure 11, *i.e.* less impact for larger particles which tend to have lower volatile mass fraction. Thus, this agreement between two completely independent characterization methods (chemical versus physical) indicates the reliability of the performed on-line measurements and validates the main conclusions drawn from their results.

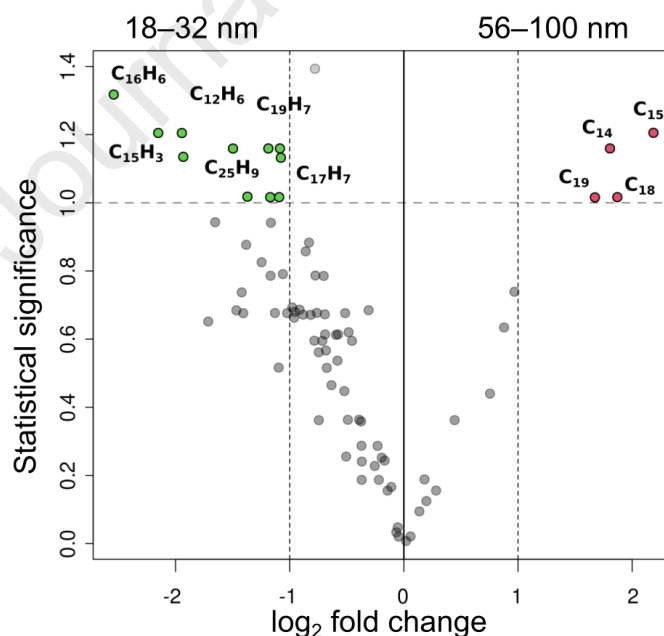


Figure 12: Volcano plot for mass spectra of particles collected in the 18–32 nm and 56–100 nm size-bins. The data for all detected species are plotted as \log_2 fold change (x -axis) versus the $-\log_{10}$ of the adjusted p -value (statistical significance, y -axis). The threshold for the statistical significance (dashed horizontal line) corresponds to a p -value of 0.1. Green symbols indicate species that have a higher contribution to mass spectra of smaller particles (18–32 nm) while red markers display chemical compounds that are predominantly associated with larger particles (56–100 nm). Chemical formulas associated with some chemical species are indicated.

5. Conclusions

A tandem arrangement of AAC, DMA, optional CS, CPMA, and CPC was used to measure the effective density, dynamic shape factor, and volatility of non-spherical and/or non-homogeneous particles from a GDI engine. About half of the number of particles were completely semi-volatile, while the rest had non-volatile cores with or without coating. Externally mixed semi-volatile particles accounted for 70% of the total mass of aerosol, while internally mixed semi-volatiles (as coating on soot particles) were less significant (< 1%). About 30% of the total mass was due to non-volatile particles. The mass-mobility exponent of polydisperse non-stripped particles was between that of semi-volatile droplets and stripped soot particles, which was supported by the combination of external and internal mixing between semi-volatile and soot particles. The higher mass-mobility exponent of stripped particles (2.78) was attributed to the higher volatile mass fraction of soot particles due to the lack of a catalytic converter, which resulted in the internally mixed soot particles restructuring into compact aggregates upon evaporation of the semi-volatile component. The compact structure of stripped particles in this study was also observed in higher effective density values and less dependence on particle mobility diameter.

Classification of non-spherical particles, unlike spherical particles, can be challenging as monodisperse particles in one property (*e.g.* aerodynamic diameter) are not monodisperse in other properties (*e.g.* mobility diameter or mass). A key endeavor in this study was to compare the effective density and dynamic shape factor when monodisperse particles are generated by various classification approaches. The effective density of monodisperse particles agreed within the uncertainty using DMA-CPMA, AAC-DMA, and AAC-CPMA tandem methods; however, the latter method generally had larger discrepancy with the other two methods for non-spherical particles. This was attributed to the non-spherical particles with a wide range of masses having the same aerodynamic diameter and thus be selected by the AAC

concurrently. The theory and the propagation of uncertainty showed that the AAC-CPMA method has the highest uncertainty in determining the effective density compared to the other two methods.

The CPMA and AAC-DMA measurements resulted in similar values for the volume equivalent diameter of non-stripped and stripped particles. For the stripped particles with a compact structure, the volume equivalent diameter of stripped particles was ~ 0.8 of their mobility diameter. Both AAC-CPMA and DMA-CPMA methods gave statistically similar values for the dynamic shape factor of larger particles, however, the dynamic shape factor based on the DMA-CPMA method was not physically reasonable for small particles. The volatile mass fraction of particles decreased as the particle mobility diameter increased, indicating that the smaller particles had a higher volatile mass fraction (up to $\sim 25\%$) on them. A similar conclusion was obtained from chemical characterization of size-selected particles which revealed that the smallest analyzed particles (10–32 nm) contained the largest volatile mass fraction. It is noteworthy that the agreement between chemical characterization method and tandem measurements with aerosol instruments implies the reliability of the latter. Thus, on-line aerosol instruments (such as DMA-CS-CPMA) can be a reliable alternative to off-line methods in the study of PM emissions volatility.

CRedit authorship contribution statement

Mohsen Kazemimanesh: Original draft writing, Investigation, Formal analysis, Visualization, Data curation. **Md Mustafizur Rahman:** Investigation, Formal analysis. **Dimitru Duca:** Investigation, Formal analysis. **Tyler J. Johnson:** Investigation, Review & editing. **Ahmed Addad:** Investigation. **George Giannopoulos:** Review & editing. **Cristian Focsa:** Supervision, Conceptualization, Methodology, Resources, Funding acquisition, Review & editing. **Adam M. Boies:** Supervision, Conceptualization, Methodology, Resources, Funding acquisition, Review & editing.

Acknowledgement

The authors wish to acknowledge contributions of equipment and time from our PEMS4Nano partners, Bosch GmbH, TSI Inc. and Horiba Ltd. The TEM facility in Lille, France is supported by the Conseil Régional des Hauts-de-France and the European Regional Development Fund (ERDF).

Funding

This project has received funding as a part of the PEMS4Nano project from the European Union's Horizon 2020 research and innovation programme under Grant Agreement no. 724145. Additionally, this work was supported by the UK EPSRC Centre for Sustainable Road Freight (EP/R035199/1) and NERC Integrated Research Observation System for Clean Air (NE/T001909/1).

References

- Adachi, K., & Buseck, P. R. (2008). Internally mixed soot, sulfates, and organic matter in aerosol particles from Mexico City. *Atmospheric Chemistry and Physics*, 8(21), 6469–6481. <https://doi.org/10.5194/acp-8-6469-2008>
- Bambha, R. P., Dansson, M. A., Schrader, P. E., & Michelsen, H. A. (2013). Effects of volatile coatings and coating removal mechanisms on the morphology of graphitic soot. *Carbon*, 61, 80–96. <https://doi.org/10.1016/j.carbon.2013.04.070>
- Barone, T. L., Lall, A. A., Storey, J. M. E., Mulholland, G. W., Prikhodko, V. Y., Frankland, J. H., Parks, J. E., & Zachariah, M. R. (2011). Size-Resolved Density Measurements of Particle Emissions from an Advanced Combustion Diesel Engine: Effect of Aggregate Morphology. *Energy & Fuels*, 25(5), 1978–1988. <https://doi.org/10.1021/ef200084k>
- Bérubé, K. A., Jones, T. P., Williamson, B. J., Winters, C., Morgan, A. J., & Richards, R. J. (1999). Physicochemical characterisation of diesel exhaust particles: Factors for assessing biological activity. *Atmospheric Environment*, 33(10), 1599–1614. [https://doi.org/10.1016/S1352-2310\(98\)00384-7](https://doi.org/10.1016/S1352-2310(98)00384-7)
- Bond, T. C., Doherty, S. J., Fahey, D. W., Forster, P. M., Berntsen, T., Deangelo, B. J., Flanner, M. G., Ghan, S., Kärcher, B., Koch, D., Kinne, S., Kondo, Y., Quinn, P. K., Sarofim, M. C., Schultz, M. G., Schulz, M., Venkataraman, C., Zhang, H., Zhang, S., ... Zender, C. S. (2013). Bounding the role of black carbon in the climate system: A scientific assessment. *Journal of Geophysical Research Atmospheres*, 118(11), 5380–5552. <https://doi.org/10.1002/jgrd.50171>
- Cappa, C. D., Onasch, T. B., Massoli, P., Worsnop, D. R., Bates, T. S., Cross, E. S., Davidovits, P., Hakala, J., Hayden, K. L., Jobson, B. T., Kolesar, K. R., Lack, D. A., Lerner, B. M., Li, S. M., Mellon, D., Nuaaman, I., Olfert, J. S., Petäjä, T., Quinn, P. K., ... Zaveri, R. A. (2012). Radiative absorption enhancements due to the mixing state of atmospheric black carbon. *Science*, 337(6098), 1078–1081. <https://doi.org/10.1126/science.1223447>
- Chakrabarty, R. K., & Heinson, W. R. (2018). Scaling Laws for Light Absorption Enhancement

- Due to Nonrefractory Coating of Atmospheric Black Carbon Aerosol. *Physical Review Letters*, 121(21), 218701. <https://doi.org/10.1103/PhysRevLett.121.218701>
- China, S., Mazzoleni, C., Gorkowski, K., Aiken, A. C., & Dubey, M. K. (2013). Morphology and mixing state of individual freshly emitted wildfire carbonaceous particles. *Nature Communications*, 4(1), 1–7. <https://doi.org/10.1038/ncomms3122>
- Collura, S., Chaoui, N., Azambre, B., Fingueneisel, G., Heintz, O., Krzton, A., Koch, A., & Weber, J. V. (2005). Influence of the soluble organic fraction on the thermal behaviour, texture and surface chemistry of diesel exhaust soot. *Carbon*, 43(3), 605–613. <https://doi.org/10.1016/j.carbon.2004.10.026>
- Cross, E. S., Onasch, T. B., Ahern, A., Wrobel, W., Slowik, J. G., Olfert, J., Lack, D. A., Massoli, P., Cappa, C. D., Schwarz, J. P., Spackman, J. R., Fahey, D. W., Sedlacek, A., Trimborn, A., Jayne, J. T., Freedman, A., Williams, L. R., Ng, N. L., Mazzoleni, C., ... Davidovits, P. (2010). Soot Particle Studies—Instrument Inter-Comparison—Project Overview. *Aerosol Science and Technology*, 44(8), 592–611. <https://doi.org/10.1080/02786826.2010.482113>
- DeCarlo, P. F., Slowik, J. G., Worsnop, D. R., Davidovits, P., & Jimenez, J. L. (2004). Particle morphology and density characterization by combined mobility and aerodynamic diameter measurements. Part 1: Theory. *Aerosol Science and Technology*, 38(12), 1185–1205. <https://doi.org/10.1080/027868290903907>
- Di Iorio, S., Catapano, F., Magno, A., Sementa, P., & Vaglieco, B. M. (2021). Investigation on sub-23 nm particles and their volatile organic fraction (VOF) in PFI/DI spark ignition engine fueled with gasoline, ethanol and a 30 %v/v ethanol blend. *Journal of Aerosol Science*, 153, 105723. <https://doi.org/10.1016/j.jaerosci.2020.105723>
- Dickau, M., Olfert, J., Stettler, M. E. J., Boies, A., Momenimovahed, A., Thomson, K., Smallwood, G., & Johnson, M. (2016). Methodology for quantifying the volatile mixing state of an aerosol. *https://Doi.Org/10.1080/02786826.2016.1185509*, 50(8), 759–772. <https://doi.org/10.1080/02786826.2016.1185509>
- Duca, D., Irimiea, C., Faccinnetto, A., Noble, J. A., Vojkovic, M., Carpentier, Y., Ortega, I. K., Pirim, C., & Focsa, C. (2019). On the benefits of using multivariate analysis in mass spectrometric studies of combustion-generated aerosols. *Faraday Discussions*, 218, 115–137. <https://doi.org/10.1039/c8fd00238j>

- Duca, D., Rahman, M., Carpentier, Y., Pirim, C., Boies, A. M., & Focsa, C. (2021). Chemical characterization of size-selected nanoparticles emitted by a gasoline direct injection engine: impact of a catalytic stripper. *Fuel*, *In press*.
- Faccinetto, A., Focsa, C., Desgroux, P., & Ziskind, M. (2015). Progress toward the Quantitative Analysis of PAHs Adsorbed on Soot by Laser Desorption/Laser Ionization/Time-of-Flight Mass Spectrometry. *Environmental Science and Technology*, *49*(17), 10510–10520. <https://doi.org/10.1021/acs.est.5b02703>
- Funkenbusch, E. F., Leddy, D. G., & Johnson, J. H. (1979). The Characterization of the Soluble Organic Fraction of Diesel Particulate Matter. *SAE Transactions*, *88*, 1540–1560. <https://www.jstor.org/stable/44658164>
- Gaffney, J. S., & Marley, N. A. (2009). The impacts of combustion emissions on air quality and climate - From coal to biofuels and beyond. *Atmospheric Environment*, *43*(1), 23–36. <https://doi.org/10.1016/j.atmosenv.2008.09.016>
- Ghazi, R., & Olfert, J. S. (2013). Coating Mass Dependence of Soot Aggregate Restructuring due to Coatings of Oleic Acid and Dioctyl Sebacate. *Aerosol Science and Technology*, *47*(2), 192–200. <https://doi.org/10.1080/02786826.2012.741273>
- Ghazi, R., Tjong, H., Soewono, A., Rogak, S. N., & Olfert, J. S. (2013). Mass, Mobility, Volatility, and Morphology of Soot Particles Generated by a McKenna and Inverted Burner. *Aerosol Science and Technology*, *47*(4), 395–405. <https://doi.org/10.1080/02786826.2012.755259>
- Grahame, T. J., Klemm, R., & Schlesinger, R. B. (2014). Public health and components of particulate matter: The changing assessment of black carbon. *Journal of the Air & Waste Management Association*, *64*(6), 620–660. <https://doi.org/10.1080/10962247.2014.912692>
- Graves, B. M., Johnson, T. J., Nishida, R. T., Dias, R. P., Savareear, B., Harynuk, J. J., Kazemimanesh, M., Olfert, J. S., & Boies, A. M. (2020). Comprehensive characterization of mainstream marijuana and tobacco smoke. *Scientific Reports*, *10*(7160). <https://doi.org/10.1038/s41598-020-63120-6>
- Graves, B. M., Koch, C. R., & Olfert, J. S. (2017). Morphology and volatility of particulate matter emitted from a gasoline direct injection engine fuelled on gasoline and ethanol blends. *Journal of Aerosol Science*, *105*, 166–178.

<https://doi.org/10.1016/J.JAEROSCI.2016.10.013>

- Graves, B. M., Olfert, J. S., Patychuk, B., Dastanpour, R., & Rogak, S. N. (2015). Characterization of Particulate Matter Morphology and Volatility from a Compression-Ignition Natural-Gas Direct-Injection Engine. *Aerosol Science and Technology*, *49*(8), 589–598. <https://doi.org/10.1080/02786826.2015.1050482>
- Gu, X., Huang, Z., Cai, J., Gong, J., Wu, X., & Lee, C. F. (2012). Emission characteristics of a spark-ignition engine fuelled with gasoline-n-butanol blends in combination with EGR. *Fuel*, *93*, 611–617. <https://doi.org/10.1016/j.fuel.2011.11.040>
- Hinds, W. C. (1999). *Aerosol Technology: Properties, Behavior, and Measurement of Airborne Particles* (2nd ed.). John Wiley & Sons.
- Jacobson, M. Z. (2001). Strong radiative heating due to the mixing state of black carbon in atmospheric aerosols. *Nature*, *409*(6821), 695–697. <https://doi.org/10.1038/35055518>
- Janssen, N. A. H., Hoek, G., Simic-Lawson, M., Fischer, P., van Bree, L., ten Brink, H., Keuken, M., Atkinson, R. W., Anderson, H. R., Brunekreef, B., & Cassee, F. R. (2011). Black Carbon as an Additional Indicator of the Adverse Health Effects of Airborne Particles Compared with PM₁₀ and PM_{2.5}. *Environmental Health Perspectives*, *119*(12), 1691–1699. <https://doi.org/10.1289/ehp.1003369>
- Johnson, T. J., Irwin, M., Symonds, J. P. R., Olfert, J. S., & Boies, A. M. (2018). Measuring aerosol size distributions with the aerodynamic aerosol classifier. *Aerosol Science and Technology*, *52*(6), 655–665. <https://doi.org/10.1080/02786826.2018.1440063>
- Johnson, T. J., Nishida, R. T., Zhang, X., Symonds, J. P. R., Olfert, J. S., & Boies, A. M. (2021). Generating an aerosol of homogeneous, non-spherical particles and measuring their bipolar charge distribution. *Journal of Aerosol Science*, *153*, 105705. <https://doi.org/10.1016/j.jaerosci.2020.105705>
- Johnson, T. J., Olfert, J. S., Yurteri, C. U., Cabot, R., & McAughey, J. (2015). Hygroscopic effects on the mobility and mass of cigarette smoke particles. *Journal of Aerosol Science*, *86*, 69–78. <https://doi.org/10.1016/J.JAEROSCI.2015.04.005>
- Kazemimanesh, M., Baldelli, A., Trivanovic, U., Popovicheva, O., Timofeev, M., Shonija, N., Obvintsev, Y., Kuang, C., Jefferson, A. M., Corbin, J. C., Goss, G. G., Alessi, D. S., Johnson, M. R., Rogak, S. N., & Olfert, J. S. (2021). Particulate emissions from turbulent diffusion flames with entrained droplets: A laboratory simulation of gas flaring emissions.

- Journal of Aerosol Science*, 105807. <https://doi.org/10.1016/j.jaerosci.2021.105807>
- Kazemimanesh, M., Dastanpour, R., Baldelli, A., Moallemi, A., Thomson, K. A., Jefferson, M. A., Johnson, M. R., Rogak, S. N., & Olfert, J. S. (2019). Size, effective density, morphology, and nano-structure of soot particles generated from buoyant turbulent diffusion flames. *Journal of Aerosol Science*, 132, 22–31. <https://doi.org/10.1016/j.jaerosci.2019.03.005>
- Khalizov, A. F., Hogan, B., Qiu, C., Petersen, E. L., & Zhang, R. (2012). Characterization of Soot Aerosol Produced from Combustion of Propane in a Shock Tube. *Aerosol Science and Technology*, 46(8), 925–936. <https://doi.org/10.1080/02786826.2012.683839>
- Leung, K. K., Schnitzler, E. G., Jäger, W., & Olfert, J. S. (2017). Relative Humidity Dependence of Soot Aggregate Restructuring Induced by Secondary Organic Aerosol: Effects of Water on Coating Viscosity and Surface Tension. *Environmental Science & Technology Letters*, 4(9), 386–390. <https://doi.org/10.1021/acs.estlett.7b00298>
- Lim, S. S., Vos, T., Flaxman, A. D., Danaei, G., Shibuya, K., Adair-Rohani, H., Amann, M., Anderson, H. R., Andrews, K. G., Aryee, M., Atkinson, C., Bacchus, L. J., Bahalim, A. N., Balakrishnan, K., Balmes, J., Barker-Collo, S., Baxter, A., Bell, M. L., Blore, J. D., ... Ezzati, M. (2012). A comparative risk assessment of burden of disease and injury attributable to 67 risk factors and risk factor clusters in 21 regions, 1990-2010: A systematic analysis for the Global Burden of Disease Study 2010. *The Lancet*, 380(9859), 2224–2260. [https://doi.org/10.1016/S0140-6736\(12\)61766-8](https://doi.org/10.1016/S0140-6736(12)61766-8)
- Liu, S., Aiken, A. C., Gorkowski, K., Dubey, M. K., Cappa, C. D., Williams, L. R., Herndon, S. C., Massoli, P., Fortner, E. C., Chhabra, P. S., Brooks, W. A., Onasch, T. B., Jayne, J. T., Worsnop, D. R., China, S., Sharma, N., Mazzoleni, C., Xu, L., Ng, N. L., ... Prévôt, A. S. H. (2015). Enhanced light absorption by mixed source black and brown carbon particles in UK winter. *Nature Communications* 2015 6:1, 6(1), 1–10. <https://doi.org/10.1038/ncomms9435>
- Maricq, M. M. (2007). Chemical characterization of particulate emissions from diesel engines: A review. *Journal of Aerosol Science*, 38(11), 1079–1118. <https://doi.org/10.1016/j.jaerosci.2007.08.001>
- McMurry, P. H., Wang, X., Park, K., & Ehara, K. (2002). The Relationship between Mass and Mobility for Atmospheric Particles: A New Technique for Measuring Particle Density.

- Aerosol Science and Technology*, 36(2), 227–238.
<https://doi.org/10.1080/027868202753504083>
- Momenimovahed, A., & Olfert, J. S. (2015). Effective Density and Volatility of Particles Emitted from Gasoline Direct Injection Vehicles and Implications for Particle Mass Measurement. *Aerosol Science and Technology*, 49(11), 1051–1062.
<https://doi.org/10.1080/02786826.2015.1094181>
- Ngo, L. D., Duca, D., Carpentier, Y., Noble, J. A., Ikhenazene, R., Vojkovic, M., Irimiea, C., Ortega, I. K., Lefevre, G., Yon, J., Faccinetto, A., Therssen, E., Ziskind, M., Chazallon, B., Pirim, C., & Focsa, C. (2020). Chemical discrimination of the particulate and gas phases of miniCAST exhausts using a two-filter collection method. *Atmospheric Measurement Techniques*, 13(2), 951–967. <https://doi.org/10.5194/amt-13-951-2020>
- Olfert, J. S., & Rogak, S. (2019). Universal relations between soot effective density and primary particle size for common combustion sources. *Aerosol Science and Technology*, 53(5), 485–492. <https://doi.org/10.1080/02786826.2019.1577949>
- Olfert, J. S., Symonds, J. P. R., & Collings, N. (2007). The effective density and fractal dimension of particles emitted from a light-duty diesel vehicle with a diesel oxidation catalyst. *Journal of Aerosol Science*, 38(1), 69–82.
<https://doi.org/10.1016/J.JAEROSCI.2006.10.002>
- Ouf, F. X., Bourrous, S., Fauvel, S., Kort, A., Lintis, L., Nuvoli, J., & Yon, J. (2019). True density of combustion emitted particles: A comparison of results highlighting the influence of the organic contents. *Journal of Aerosol Science*, 134, 1–13.
<https://doi.org/10.1016/j.jaerosci.2019.04.007>
- Pagels, J., Khalizov, A. F., McMurry, P. H., & Zhang, R. Y. (2009). Processing of Soot by Controlled Sulphuric Acid and Water Condensation—Mass and Mobility Relationship. *Aerosol Science and Technology*, 43(7), 629–640.
<https://doi.org/10.1080/02786820902810685>
- Park, K., Cao, F., Kittelson, D. B., & McMurry, P. H. (2003). Relationship between Particle Mass and Mobility for Diesel Exhaust Particles. *Environmental Science & Technology*, 37(3), 577–583. <https://doi.org/10.1021/es025960v>
- Park, K., Kittelson, D. B., & McMurry, P. H. (2004). Structural Properties of Diesel Exhaust Particles Measured by Transmission Electron Microscopy (TEM): Relationships to

- Particle Mass and Mobility. *Aerosol Science and Technology*, 38(9), 881–889. <https://doi.org/10.1080/027868290505189>
- Peng, J., Hu, M., Guo, S., Du, Z., Zheng, J., Shang, D., Zamora, M. L., Zeng, L., Shao, M., Wu, Y. S., Zheng, J., Wang, Y., Glen, C. R., Collins, D. R., Molina, M. J., & Zhang, R. (2016). Markedly enhanced absorption and direct radiative forcing of black carbon under polluted urban environments. *Proceedings of the National Academy of Sciences of the United States of America*, 113(16), 4266–4271. <https://doi.org/10.1073/pnas.1602310113>
- Quiros, D. C., Hu, S., Hu, S., Lee, E. S., Sardar, S., Wang, X., Olfert, J. S., Jung, H. S., Zhu, Y., & Huai, T. (2015). Particle effective density and mass during steady-state operation of GDI, PFI, and diesel passenger cars. *Journal of Aerosol Science*, 83, 39–54. <https://doi.org/10.1016/J.JAEROSCI.2014.12.004>
- Ramanathan, V., & Carmichael, G. (2008). Global and regional climate changes due to black carbon. *Nature Geoscience*, 1(4), 221–227. <https://doi.org/10.1038/ngeo156>
- Ristimäki, J., Vaaraslahti, K., Lappi, M., & Keskinen, J. (2007). Hydrocarbon Condensation in Heavy-Duty Diesel Exhaust. *Environmental Science & Technology*, 41(18), 6397–6402. <https://doi.org/10.1021/es0624319>
- Sakurai, H., Tobias, H. J., Park, K., Zarling, D., Docherty, K. S., Kittelson, D. B., McMurry, P. H., & Ziemann, P. J. (2003). On-line measurements of diesel nanoparticle composition and volatility. *Atmospheric Environment*, 37(9–10), 1199–1210. [https://doi.org/10.1016/S1352-2310\(02\)01017-8](https://doi.org/10.1016/S1352-2310(02)01017-8)
- Schauer, J. J., Kleeman, M. J., Cass, G. R., & Simoneit, B. R. T. (1999). Measurement of emissions from air pollution sources. 2. C1 through C30 organic compounds from medium duty diesel trucks. *Environmental Science and Technology*, 33(10), 1578–1587. <https://doi.org/10.1021/es980081n>
- Schmitt-Kopplin, P., Gelencsér, A., Dabek-Zlotorzynska, E., Kiss, G., Hertkorn, N., Harir, M., Hong, Y., & Gebefügi, I. (2010). Analysis of the unresolved organic fraction in atmospheric aerosols with ultrahigh-resolution mass spectrometry and nuclear magnetic resonance spectroscopy: Organosulfates as photochemical smog constituents. *Analytical Chemistry*, 82(19), 8017–8026. <https://doi.org/10.1021/ac101444r>
- Schnitzler, E. G., Dutt, A., Charbonneau, A. M., Olfert, J. S., & Jäger, W. (2014). Soot aggregate restructuring due to coatings of secondary organic aerosol derived from

- aromatic precursors. *Environmental Science and Technology*, 48(24), 14309–14316. <https://doi.org/10.1021/es503699b>
- Slowik, J. G., Cross, E. S., Han, J. H., Davidovits, P., Onasch, T. B., Jayne, J. T., Williams, L. R., Canagaratna, M. R., Worsnop, D. R., Chakrabarty, R. K., Moosmüller, H., Arnott, W. P., Schwarz, J. P., Gao, R. S., Fahey, D. W., Kok, G. L., & Petzold, A. (2007). An Inter-Comparison of Instruments Measuring Black Carbon Content of Soot Particles. *Aerosol Science and Technology*, 41(3), 295–314. <https://doi.org/10.1080/02786820701197078>
- Slowik, J. G., Cross, E. S., Han, J. H., Kolucki, J., Davidovits, P., Williams, L. R., Onasch, T. B., Jayne, J. T., Kolb, C. E., & Worsnop, D. R. (2007). Measurements of morphology changes of fractal soot particles using coating and denuding experiments: Implications for optical absorption and atmospheric lifetime. *Aerosol Science and Technology*, 41(8), 734–750. <https://doi.org/10.1080/02786820701432632>
- Slowik, J. G., Stainken, K., Davidovits, P., Williams, L. R., Jayne, J. T., Kolb, C. E., Worsnop, D. R., Rudich, Y., DeCarlo, P. F., & Jimenez, J. L. (2004). Particle morphology and density characterization by combined mobility and aerodynamic diameter measurements. Part 2: Application to combustion-generated soot aerosols as a function of fuel equivalence ratio. *Aerosol Science and Technology*, 38(12), 1206–1222. <https://doi.org/10.1080/027868290903916>
- Storey, J. M., Barone, T., Norman, K., & Lewis, S. (2010). Ethanol blend effects on direct injection spark-ignition gasoline vehicle particulate matter emissions. *SAE International Journal of Fuels and Lubricants*, 3(2), 650–659. <https://doi.org/10.4271/2010-01-2129>
- Tavakoli, F., & Olfert, J. S. (2014). Determination of particle mass, effective density, mass-mobility exponent, and dynamic shape factor using an aerodynamic aerosol classifier and a differential mobility analyzer in tandem. *Journal of Aerosol Science*, 75, 35–42. <https://doi.org/10.1016/j.jaerosci.2014.04.010>
- Thamban, N. M., Tripathi, S. N., Moosakutty, S. P., Kuntamukkala, P., & Kanawade, V. P. (2017). Internally mixed black carbon in the Indo-Gangetic Plain and its effect on absorption enhancement. *Atmospheric Research*, 197, 211–223. <https://doi.org/10.1016/J.ATMOSRES.2017.07.007>
- Trivanovic, U., Sipkens, T. A., Kazemimanesh, M., Baldelli, A., Jefferson, A. M., Conrad, B. M., Johnson, M. R., Corbin, J. C., Olfert, J. S., & Rogak, S. N. (2020). Morphology and

- size of soot from gas flares as a function of fuel and water addition. *Fuel*, 279, 118478. <https://doi.org/10.1016/j.fuel.2020.118478>
- Wang, S. C., & Flagan, R. C. (1990). Scanning electrical mobility spectrometer. *Aerosol Science and Technology*, 13(2), 230–240. <https://doi.org/10.1080/02786829008959441>
- Wang, X., Grose, M. A., Caldow, R., Osmondson, B. L., Swanson, J. J., Chow, J. C., Watson, J. G., Kittelson, D. B., Li, Y., Xue, J., Jung, H., & Hu, S. (2016). Improvement of Engine Exhaust Particle Sizer (EEPS) size distribution measurement - II. Engine exhaust particles. *Journal of Aerosol Science*, 92, 83–94. <https://doi.org/10.1016/j.jaerosci.2015.11.003>
- Xue, H., Khalizov, A. F., Wang, L., Zheng, J., & Zhang, R. (2009). Effects of Coating of Dicarboxylic Acids on the Mass–Mobility Relationship of Soot Particles. *Environmental Science & Technology*, 43(8), 2787–2792. <https://doi.org/10.1021/es803287v>
- Yao, Q., Asa-Awuku, A., Zangmeister, C. D., & Radney, J. G. (2020). Comparison of three essential sub-micrometer aerosol measurements: Mass, size and shape. *Aerosol Science and Technology*, 54(10), 1197–1209. <https://doi.org/10.1080/02786826.2020.1763248>
- Zhang, Z., Wang, T., Jia, M., Wei, Q., Meng, X., & Shu, G. (2014). Combustion and particle number emissions of a direct injection spark ignition engine operating on ethanol/gasoline and n-butanol/gasoline blends with exhaust gas recirculation. *Fuel*, 130, 177–188. <https://doi.org/10.1016/j.fuel.2014.04.052>

Highlights

- A comparison of particle effective density and shape factor using tandem AAC, DMA, and CPMA is presented.
- Particle effective density using DMA-CPMA, AAC-DMA, and AAC-CPMA was consistent.
- The AAC-CPMA method had larger discrepancy with the other two methods.
- Dynamic shape factor (by AAC-CPMA and DMA-CPMA) increased with mobility diameter.
- Volatile mass fraction of particles decreased as their mobility diameter increased.

Declaration of interests

The authors declare that they have no known competing financial interests or personal relationships that could have appeared to influence the work reported in this paper.

The authors declare the following financial interests/personal relationships which may be considered as potential competing interests:

Journal Pre-proof